Particuology 115 (2026) 157–173

Contents lists available at ScienceDirect

Particuology

journal homepage: www.elsevier.com/locate/partic

CFD-DEM investigation on particle erosion characteristics of shaftless rim-driven thruster in sediment-laden flow

Nan Wang[a], Zhentao Wang[a,b,*], Bin Li[a], Qingming Dong[a], Junfeng Wang[a,c], Jiyuan Tu[b,d]

[a] School of Energy and Power Engineering, Jiangsu University, Zhenjiang, 212013, China
[b] Key Laboratory of Advanced Reactor Engineering and Safety, Ministry of Education, Tsinghua University, Beijing, 100084, China
[c] School of Energy and Power Engineering, Chongqing University, Chongqing, 400044, China
[d] School of Engineering, RMIT University, Victoria, 3083, Australia

HIGHLIGHTS

- Larger particles intensify erosion at blade edges, while smaller cause uniform wear.
- Barley-shaped particles cause stronger erosion and higher efficiency loss than sphere.
- More blades and higher r/R improve flow uniformity and reduce wear.

GRAPHICAL ABSTRACT

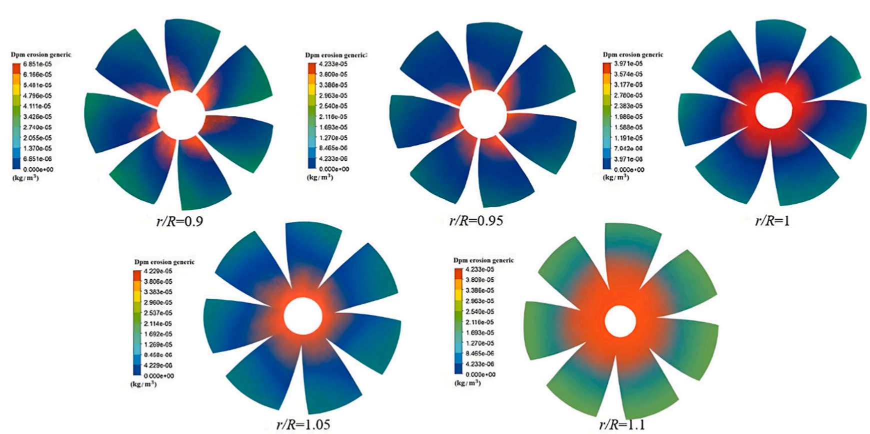

Surface article erosion with various r/R

ARTICLE INFO

Keywords:
CFD-DEM method
Particle erosion
Shaftless rim-driven thruster
Hydrodynamic performance
Multiphase flow

ABSTRACT

This study investigates particles erosion characteristics of shaftless rim-driven thrusters (RDTs) adopting CFD-DEM method. A three-dimensional RDTs model was developed to evaluate the effect of particles size, shape, and flow rate on erosion pattern and hydrodynamic performance. The results indicate that larger particles could induce severe localized erosion at blade leading edge owing to the higher inertia, whereas smaller particles generate more uniform but milder wear. Mixed particles distribution can produce combined effect, resembling actual sediment-laden environments. Moreover, blade number and hub-to-tip ratio also markedly influence erosion. The fewer blades and smaller r/R values lead to concentrated erosion, and increasing blade number and r/R enhances flow uniformity and reduces wear. The comparison between spherical and irregular (barley-shaped) particles reveal that irregular morphology causes stronger localized erosion and greater efficiency losses. In addition, higher particle mass flow rate intensifies erosion, expanding the affected regions from localized hotspots to entire blade surfaces.

* Corresponding author. School of Energy and Power Engineering, Jiangsu University, Zhenjiang 212013, China.
E-mail address: zhentao.wang@ujs.edu.cn (Z. Wang).

https://doi.org/10.1016/j.partic.2026.05.012
Received 12 March 2026; Received in revised form 8 May 2026; Accepted 15 May 2026
Available online 22 May 2026

1. Introduction

Shaftless rim-driven thruster (RDTs), as an emerging type of propulsion system, have attracted much attention due to compact configuration, low noise, and high reliability compared with conventional shaft-driven propellers (Nie et al., 2023). RDTs eliminate the mechanical transmission shaft and instead rely on electromagnetic or hydraulic drives to deliver torque directly to the propeller rim. This unique structure design greatly enables flexible installation, simplifies sealing arrangements, and substantially reduces vibration and maintenance requirements. Furthermore, the removal of central shaft opens additional flow area, thereby improving hydrodynamic efficiency and promoting much quieter and more stable operation. These advantages position RDTs as a promising alternative for industrial applications where compactness, environmental resilience and operational reliability are critical, such as in unmanned underwater vehicles, electric ships and aerospace propulsion systems.

However, RDTs often operate in environments laden with solid particles such as sand, dust or salt crystals, which can significantly threaten the performance and produce potential damage. Particle erosion refers to the progressive material removal that occurs when solid particles suspended in carrier fluid impact the surface of component at high velocity (Yan et al., 2017). This phenomenon is widely observed in aerospace turbines, hydraulic machinery and marine propulsion devices exposed to sediment-laden or contaminated flows. The impacting energy of entrained particles can induce surface pitting, micro-cutting and fatigue cracking, gradually deteriorating surface integrity and leading to efficiency losses or structural failure (Cao et al., 2015). In propulsion systems, such degradation not only affects thrust performance but also increases energy consumption, maintenance frequency and operational risks, especially under high-speed or long-duration operation.

Despite the structural innovations, RDTs are not immune to erosion. The rim-driven configuration inherently involves thin blade tip and an enclosed annular channel, which are particularly susceptible to particle impacts. When operating in harsh environments such as muddy rivers, turbid waters or dust-filled atmospheres, the relative velocity between the rotating blades and suspended particles become extremely high near the blade tip. Consequently, localized wear, especially at the leading and trailing edges of the rim, can intensify rapidly, compromising both hydrodynamic performance and structural stability. Moreover, since RDTs rely on compact electromagnetic drives integrated into the rim, even minor material loss may lead to unbalanced loading or electromagnetic misalignment, further accelerating performance degradation. This makes it essential to understand erosion mechanisms specific to RDTs and to develop effective design strategy for mitigating erosion in such system (Suryanarayana et al., 2010; Yakovlev et al., 2011).

To enhance the erosion resistance of propulsion components, a variety of mitigation strategies have been developed. Surface strengthening techniques, such as thermal spraying, hard coatings and laser surface treatment, have demonstrated substantial improvements in hardness and wear resistance (Lai, 2006). Electroplating and chemical vapor deposition can further reduce surface roughness, minimizing particle adherence and secondary abrasion (Cao et al., 2012; Chen, Wang, & Hua, 2017). From design perspective, optimizing the hydrodynamic characteristics of the flow field plays a critical role. By tailoring blade geometry including camber, pitch angle and leading-edge curvature, particles trajectories can be redirected, thereby reducing direct impingement on vulnerable surfaces (Cheng et al., 2024). Similarly, adjustments in the hub-to-tip ratio and rim channel geometry can influence local pressure gradients and turbulence intensity, effectively mitigating localized erosion (Gao et al., 2025). Since particles motion is highly dependent on the surrounding flow field, the accurate understanding of internal flow behavior is fundamental to improve erosion resistance and extend system longevity.

The relation between internal flow field and erosion mechanism has been traditionally studied by experiments and numerical simulations. Experimental methods such as high-speed photography, particle image velocimetry (PIV) and laser Doppler anemometry (LDA) can provide direct visualization of multiphase flow behavior and erosion evolution (Xiao et al., 2025). These techniques have been successfully applied in turbines and centrifugal pumps to capture velocity distributions, turbulence intensities and surface wear patterns (Wang et al., 2025). However, experimental setups often face significant limitations, such as high operational costs, restricted observation regions, complex boundary conditions and difficulty reproducing microscale particle surface interactions (Pu et al., 2024). These challenges restrict the ability to reveal detailed erosion mechanisms under variable operating conditions.

In contrast, numerical simulations can offer a powerful alternative. Computational Fluid Dynamics (CFD) based on Reynolds-averaged Navier-Stokes (RANS) equations, and particularly CFD-DEM method (coupling CFD with the Discrete Element Method), enables detailed analysis of liquid-particles two-phase interactions (Inoue et al., 2025). CFD–DEM method allows direct tracking of individual particles trajectories and collisions, enabling prediction of impacting velocity, frequency and incident angle, which are critical parameters determining erosion severity (Peng et al., 2023). It is clearly indicated that numerical methods can provide efficient and flexible means to investigate the effect of operational variables such as particles size, concentration and inlet velocity on erosion characteristics (Yasser, Zhou, & El-Emam, 2025a, 2025b). They also facilitate parametric studies to optimize structural design for reduced wear. Consequently, CFD-DEM method has emerged as one of the most effective tools for studying particle-induced erosion in hydraulic and propulsion systems (Ko et al., 2025; Yasser et al., 2025a, 2025b).

Recent investigations into centrifugal pumps and pipeline systems have demonstrated the capabilities of numerical modeling in predicting erosion mechanisms and performance degradation. Studies employing RANS-based CFD and CFD-DEM coupling frameworks have analyzed the effect of particles concentration, velocity and size on erosion distribution and flow stability (Adachi et al., 2024; Jing et al., 2024; Wang et al., 2024). High particles concentrations and large particle sizes were shown to intensify erosion near the impeller leading edge and volute tongue, leading to rapid efficiency decline. Similarly, studies on pipe bends revealed that erosion rate is primarily governed by particle velocity, followed by concentration and size, and that curvature strongly influences impact locations (Schmunk et al., 2023). Advanced erosion prediction models based on empirical fitting and grey correlation analysis have been proposed to assess erosion risk in complex flow channels (Chen et al., 2021). These models have contributed to improved understanding of the underlying relationships between turbulence, particle motion and wear distribution.

Further developments have expanded toward material performance and particle shape effects. Wang and Qian (2017) emphasized the importance of accounting for non-spherical particles in simulations, noting that polyhedral particles with sharp edges cause more severe erosion than spherical ones, which tend to underestimate actual damage. Zhai et al. (2022) and Zhang et al. (2025) reported that the choice of erosion-resistant materials, such as stainless steel and composite coatings, can significantly mitigate wear under high-strain conditions. Additionally, CFD-DEM studies have systematically analyzed how flow velocity, particle concentration and temperature influence erosion patterns, identifying flow unsteadiness and turbulence modulation as major contributors to wear localization (Karim & Ahmmed, 2012; Li et al., 2025). These findings collectively advance our understanding of erosion phenomena in conventional turbomachinery. Nevertheless, existing works primarily focuses on pumps and pipelines, while the unique flow–structure–erosion interactions in shaftless propulsion systems are still poorly understood (Zhu, 2014).

The structural and operational characteristics of RDTs present distinct challenges that differ fundamentally from traditional turbomachinery (Li et al., 2023). The rim-driven configuration produces confined annular flow passage, where the interplay between electromagnetic drive components, rotating blades and wall-bounded shear layers creates complex flow environment. The particle-laden flow exhibits strong three-dimensional motion, high turbulence intensity and pronounced secondary flows near the rim and hub regions (Xie et al., 2024). As a result, the erosion mechanism in RDTs cannot be directly inferred from those of conventional systems (Sommerfeld & Taborda, 2024). Moreover, the thin and lightweight blades required for efficient rim-driven operation are more prone to impact-induced deformation and fatigue. Consequently, the systematic investigation of the flow field and erosion behavior specific to RDTs is essential to establish accurate predictive models and design guidelines for future applications.

To address these challenges, the present study employs numerical simulation to explore the coupled flow and erosion mechanism within shaftless rim-driven thrusters. This study considers multiple influencing factors, including particles size (50 μm and 100 μm), particles shape (spherical and polyhedral) and inlet particle mass flow rate. A three-dimensional geometric model of the RDT was constructed in SolidWorks, and high-quality computational meshes were generated using ICEM. Steady and transient flow fields were solved in ANSYS Fluent based on the RANS turbulence model, while particles trajectories and impact parameters were simulated through coupling with Rocky DEM software. By analyzing flow characteristics such as pressure distribution, velocity fields and particle collision statistics, the influence of particle properties and operating conditions on erosion distribution was comprehensively evaluated. In addition, the effect of blade number and hub-to-tip ratio were also examined to identify structural configurations that enhance erosion resistance without compromising propulsion efficiency.

2. Methodology

In this work, numerical simulations were conducted to solve fluid motion, calculate particle packing and force distribution and quantify wall erosion.

2.1. Geometry model establishment

In this study, 20 kW shaftless rim-driven thruster designed for small power underwater propulsion applications in studied. It is commonly used in compact underwater vehicles, auxiliary propulsion systems and shallow-water operation platforms, where compact configuration, low vibration and high reliability are required. Compared with conventional shaft-driven propellers, the rim-driven configuration forms an enclosed annular flow passage. Therefore, when the thruster operates in sediment-laden environments, suspended solid particles can be transported into the rim channel and repeatedly impact the blade leading edge, blade tip and inner wall surfaces. The principal geometric and operating parameters of the selected RDTs were summarized in Table 1. The geometric structure of the RDTs was established by varying the thickness distribution, where r represents the radial distance of the section and R denotes the blade radius, respectively. Two-dimensional profile data were calculated and three-dimensional blade coordinates were determined using the geometric projection transformation method as expressed in Equation (1). The resulting 3D coordinate points were then imported into SOLIDWORKS to construct RDTs model. The 3D model of RDTs is illustrated in Fig. 1.

$$\begin{cases} x_{\mathrm{p}} = -[i_{\mathrm{G}} + r\theta_{\mathrm{s}}\tan(\theta_{\mathrm{nt}})] + (0.5c - x_{\mathrm{c}})\sin(\theta_{\mathrm{nt}}) + y_{\mathrm{u,l}}\cos(\theta_{\mathrm{nt}}) \\ y_{\mathrm{p}} = r\sin\left[\theta_{\mathrm{s}} - \dfrac{[(0.5c - x_{\mathrm{c}})\cos(\theta_{\mathrm{nt}}) - y_{\mathrm{u,l}}\sin(\theta_{\mathrm{nt}})]}{r}\right] \\ z_{\mathrm{p}} = r\cos\left[\theta_{\mathrm{s}} - \dfrac{[(0.5c - x_{\mathrm{c}})\cos(\theta_{\mathrm{nt}}) - y_{\mathrm{u,l}}\sin(\theta_{\mathrm{nt}})]}{r}\right] \end{cases} \tag{1}$$

Where, (x_p, y_p, z_p) is the three-dimensional coordinates of the point on the blade, r is the radius, θ_s is the skew angle, θ_{nt} is the pitch angle, i_G is the tilt angle, c is the chord length at the section, x_c is the chord length at a position x_c units away from the leading edge, and $y_{u,l}$ is the coordinate on the leaf surface and back surface at a position x_c unit away from the leading edge.

2.2. Governing equations and turbulence model

In this study, the fluid is considered as incompressible. The governing equations for mass and momentum are given in Equations (2) and (3).

$$\frac{\partial u_i}{\partial x_i} = 0 \tag{2}$$

$$\frac{\partial u_i}{\partial t} + u_j\frac{\partial u_i}{\partial x_j} = f_i - \frac{1}{\rho}\frac{\partial p}{\partial x_i} + \nu\frac{\partial^2 u_i}{\partial x_i x_j} \tag{3}$$

The Reynolds-Averaged Navier-Stokes (RANS) equations are employed to resolve the flow field:

$$\frac{\partial \overline{u}_i}{\partial x_i} = 0 \tag{4}$$

$$\frac{\partial \overline{u}_i}{\partial t} + \overline{u}_j\frac{\partial \overline{u}_i}{\partial x_j} = \overline{f}_i - \frac{1}{\rho}\frac{\partial \overline{p}}{\partial x_i} + \nu\frac{\partial^2 \overline{u}_i}{\partial x_i j} - \frac{\partial \overline{u_i' u_j'}}{\partial x_j} \tag{5}$$

Where x_i, x_j is the fluid position, ρ is the density of water, ν is the kinematic viscosity of water, p is the pressure, $\overline{p}$ is the Reynolds-averaged pressure, u_i, u_j are the velocities, $\overline{u}_i, \overline{u}_j$ $(i, j = 1, 2, 3)$ are the Reynolds-averaged velocities, f_i is the mass force, $\overline{f}_i$ is the Reynolds-averaged mass force, $\overline{u_i' u_j'}$ is the additional stress tensor after Reynolds averaging.

In this study, the Realizable $k - \varepsilon$ model is used to resolve flow turbulence (Shih et al., 1995). The transport equations for turbulent kinetic energy and the dissipation rate are shown in Equations (6) and (7):

$$\frac{\partial}{\partial t}(\rho k) + \frac{\partial}{\partial x_j}(\rho k \overline{u_j}) = \frac{\partial}{\partial x_j}\left[\left(\mu + \frac{\mu_t}{\sigma_k}\right)\frac{\partial k}{\partial x_j}\right] + G_k + G_b - \rho\varepsilon - Y_M \tag{6}$$

$$\frac{\partial}{\partial t}(\rho \varepsilon) + \frac{\partial}{\partial x_j}(\rho \varepsilon \overline{u_j}) = \frac{\partial}{\partial x_j}\left[\left(\mu + \frac{\mu_t}{\sigma_\varepsilon}\right)\frac{\partial \varepsilon}{\partial x_j}\right] + \rho C_1 S_\varepsilon - \rho C_2\frac{\varepsilon^2}{k + \sqrt{\nu\varepsilon}} \tag{7}$$

Table 1
Main parameters of the RDTs.

Parameter	Symbol	Value	Unit
Blade number	Z	4,5,6,7	-
Diameter of blade tip circle	D	260	mm
Disk area ratio	A_E/A_D	0.35	-
Pitch ratio	P/D	1	-
Slant side	$SKEW$	0	-
Ratio of pitch to diameter	Zr/D	0	-
Maximum camber ratio	f/c	0.0396	-
Rotation speed	N	720	rpm

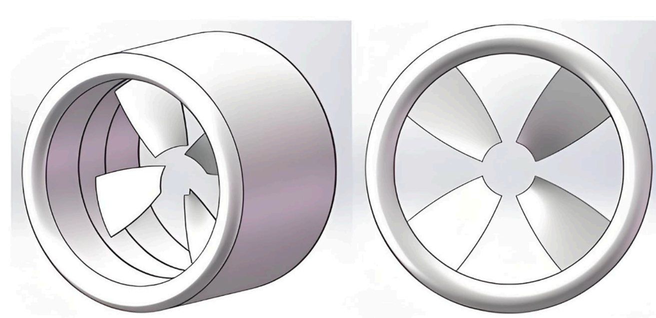

Fig. 1. The 3D model of RDTs.

Where G_k indicates the generation of turbulent kinetic energy due to the gradient of the mean velocity, G_b indicates the generation of turbulent kinetic energy due to buoyancy, Y_M shows the contribution of the undulating expansion to the overall distribution ratio in compressible turbulence. C_2 and C_1 are constants, $C_2 = 1.9$. σ_k and σ_ε are turbulent Prandtl numbers for k and ε, respectively, $\sigma_k = 1$, $\sigma_\varepsilon = 1.2$.

Solid particles are considered as discrete phase. Taking into account the physical properties of particles, the position, velocity and collision characteristics are calculated based on Newton's Second Law of Motion. The Poisson's ratio of solid particles is 0.4, the shear modulus is 21.3 MPa and the density is 1500 kg/m^3.

2.3. Multiphase model

Three principal model families are commonly employed in Fluent for multiphase flows: VOF, Mixture, and Eulerian (Vieira et al., 2024; Wu et al., 2024). VOF is designed to capture sharp interfaces between immiscible fluids, Mixture treats phases as interpenetrating continua with relative slip, and Eulerian solves full conservation equations for each phase with tight coupling. This problem features strong interphase coupling and non-uniform phase distributions and the Eulerian (Euler–Euler) framework is preferable because it is capable of resolving phase-specific conservation equations and interfacial exchanges. Accordingly, the Euler–Euler framework is adopted in this study to balance fidelity and computational cost (Hirt & Nichols, 1981).

2.4. Discretized equation solvers

Two primary strategies are employed to solve discretized algebraic systems: segregated solvers (SIMPLE, SIMPLEC and PISO) and coupled solvers. Segregated solvers decompose the system into single-variable subsystems and are efficient for weakly coupled or steady flows, whereas coupled solvers can efficiently solve the equations simultaneously and provide better fidelity for strongly coupled and highly interactive problems. Because the present problem involves strong inter-variable coupling and requires accurate interphase exchanges, the coupled solution strategy is chosen. Accordingly, the governing equation for the motion of discrete particles can be written as:

$$\frac{\mathrm{d}u_p}{\mathrm{d}t} = \frac{18\mu}{\rho_p {d_p}^2}\frac{C_D Re_p}{24}\left(u_g - u_p\right) + \frac{g_x\left(\rho_p - \rho_g\right)}{\rho_p} + f_x \tag{8}$$

$$Re_p = \frac{\rho_g d_p \left|u_g - u_p\right|}{\mu} \tag{9}$$

$$C_D = a_1 + \frac{a_2}{Re_p} + \frac{a_3}{Re_p} \tag{10}$$

Where ρ_p is the particle density, ρ_g is the density of the continuous phase, d_p is the particle diameter, C_D is the resistance coefficient, Re_p is the relative Reynolds number of particles, u_g is the continuous phase velocity, u_p is the particle velocity, f_x is the additional acceleration, g_x is the acceleration due to gravity, a_1, a_2 and a_3 are constants.

2.5. Definition of performance parameters

Several parameters are adopted to evaluate the hydrodynamic performance of RDTs, including the advance speed coefficient J, thrust coefficient K_T, torque coefficient K_Q and open water propulsion efficiency η_0. The corresponding definitions are given as follows:

$$J = \frac{V_a}{nD} \tag{11}$$

$$K_T = \frac{T}{\rho n^2 D^4} = K_{TP} + K_{TD} \tag{12}$$

$$K_Q = \frac{Q}{\rho n^2 D^5} \tag{13}$$

$$\eta_0 = \frac{K_T}{K_Q}\cdot\frac{J}{2\pi} \tag{14}$$

Where, Va is the inlet velocity, n is the rotation speed, D is the diameter, ρ is the density of fluid, T is the thrust, Q is the torque, K_{TP} is the thrust coefficient of the blades and K_{TD} is the thrust coefficient generated by the duct.

2.6. Wear model

The Oka wear model can be used for simulating material erosion of different materials. The erosion rate E_r is:

$$E_r = E_{90} g(\alpha)\left(\frac{u_{rel}}{u_{ref}}\right)^{k_1}\left(\frac{d_p}{d_{ref}}\right)^{k_2} \tag{15}$$

$$g(\alpha) = \sin^{n_1}\alpha[1 + H_v(1 - \sin\alpha)]^{n_2} \tag{16}$$

Where, E_{90} is the reference erosion rate, α is the impact angle, $g(\alpha)$ is the impact angle related function, u_{rel} is the relative velocity between the particle and the wall surface, u_{ref} is the particle reference velocity, d_{ref} is the particle reference diameter, k_1 and k_2 are specified indices, H_v is the hardness of the material, n_1 and n_2 are constants.

2.7. Wall collision rebound model

Solid particles will collide with the wall, resulting in energy loss, causing the particle reflection velocity to be lower than the incident velocity. The collision characteristics of this random particle wall rebound model are described as follows:

$$e_n = 0.993 - 0.0307\theta + 4.75\times10^{-4}\theta^2 - 2.61\times10^{-6}\theta^3 \tag{17}$$

$$e_t = 0.998 - 0.029\theta + 6.43\times10^{-4}\theta^2 - 3.56\times10^{-6}\theta^3 \tag{18}$$

Where, e_n is the normal rebound coefficient, e_t is the tangential rebound coefficient, θ is the incident angle of collision between the particle and the wall.

2.8. Boundary conditions

In this work, the computational domain is divided into stationary outer domain and rotating inner domain, as shown in Fig. 2. Static outer domain can simplify boundary conditions and reduce computational complexity, while rotating inner domain can calculate the rotational motion of RDTs. In order to reduce the influence of sliding wall conditions on the lateral boundaries and completely solve the flow field problems inside and around RDTs, 4D × 9D computational domain is adopted. According to previous research, the size of the computational domain is considered sufficiently large. The inlet with diameter of 4D is located upstream of 3D, and the outlet is located downstream of 6D. The interface between external and internal subdomains has been defined to ensure the conservation of flow mass and mechanical balance. The division and processing of high-quality grids play a crucial role in the accuracy of CFD calculations. After referring to relevant literature and considering the distribution of the computational domain, it has been decided to use cutting body grid. The rotational domain is used to simulate the rotational motion of an off-axis propeller, as illustrated in Fig. 3. The commonly used methods include the rotating reference frame (MRF) and the sliding mesh (RBM). In this paper, the MRF method is adopted, which has good computational stability and easy convergence. To ensure high grid quality, the grid size on both sides of the interface between the rotating domain and the stationary domain is equal, ensuring smooth transition of the grid and precise and stable data

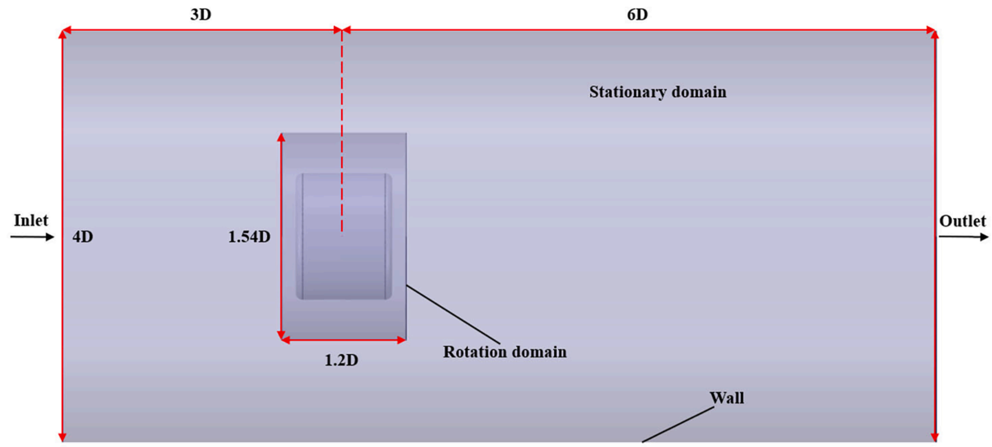

Fig. 2. Overall computational domain structure.

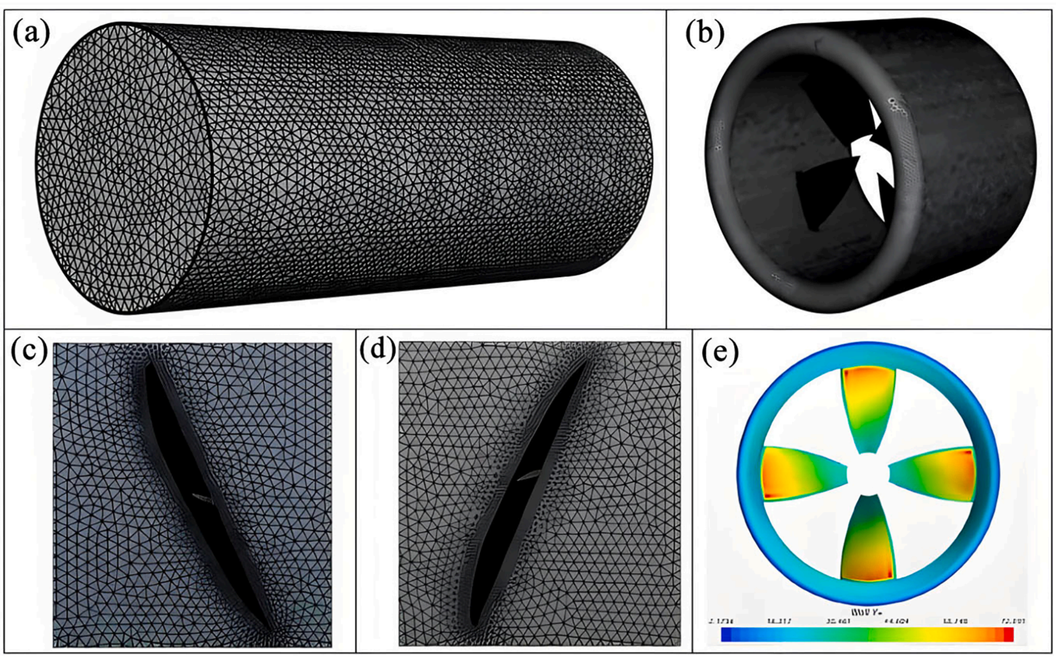

Fig. 3. Meshing of computational domain: (a) flow field; (b) Thruster; (c) Forward blade tip; (d) Aft blade tip; (e)Y-plus.

transmission. Grid refinement is applied to the surface control of the RDTs and guide tube, and line control is set at the edges of both to further optimize the grid.

In order to better capture the wake of the RDTS, a wake encryption area is set at the tail of the RDTs, using surface control and volume control. A suitable physical model and initial conditions are essential for CFD, and are set as liquid constant density in the material item. In the process of setting boundary conditions, the velocity inlet is set to the incoming flow surface of the external large cylindrical stationary domain, and the calculated velocity of the velocity inlet is set in the boundary conditions. Set the outflow surface of the external stationary domain large cylinder as the pressure outlet. The wall between the stationary domain and the rotating domain is set as a symmetrical plane, and the wall of the off-axis propeller is set as a slip free condition. In Fluent software, set the fluid to unsteady flow, and apply an escape boundary condition at the outlet for particles. The determination of the time step has a significant impact on the accuracy and efficiency of simulation results. In Fluent software, set the time step to 1×10^{-4} s. Set the calculation residual to 10^{-4}.

2.9. Model validation

To eliminate the influence of grid density on simulations, mesh sensitivity study was conducted, where five mesh configurations are adopted. The case while the J is 0.3 is adopted, the thrust coefficient and torque coefficient are used for the assessment. The results of the sensitivity study are displayed in Table 2. It can be seen that the difference of the thrust coefficient ΔK_T and the torque coefficient ΔK_Q are within 3% and 4%, respectively, indicating that the mesh configuration can reproduce the numerical data well. By balancing data accuracy and computational cost, the medium mesh with the grid number of 4.29 million is adopted for the following simulations.

This section calculated the open water performance of *Ka4-70+NO.19A* duct propeller when J = 0.1–0.9, as shown in Fig. 4, together with the comparison between calculation results and experimental values. It can be seen that the prediction of the turbulence model is relatively accurate, with the errors of open water thrust coefficient K_T and torque coefficient K_Q within 5%.

For the particle erosion prediction, direct experimental data for

Table 2
Grid independence analysis.

Configuration	Grids count	$K_{T\,Total}$	$\Delta K_{T\,Total}$	$K_{Q\,Total}$	$\Delta K_{Q\,Total}$
Very fine	12.52 million	0.1310	0	0.7300	0
Fine	8.15 million	0.1309	−0.02%	0.7283	−0.23%
Medium	4.29 million	0.1310	0.04%	0.7297	−0.06%
Coarse	2.18 million	0.1297	−0.97%	0.7205	−1.30%
Very coarse	0.94 million	0.1289	−2.60%	0.7172	−3.76%

shaftless rim-driven thrusters under sediment-laden flow are still limited because the confined annular flow passage makes local erosion measurement difficult. Although direct experimental erosion validation for the present RDTs is not available at this stage, the hydrodynamic coefficients have been quantitatively validated, and the predicted erosion trends are consistent with published particle erosion mechanism. This supports the reliability of present CFD–DEM framework for analyzing the relative influence of particles size, shape, blade number and particles mass flow rate on RDTs erosion. Nevertheless, future work will conduct controlled sediment-laden flow experiments on RDTs blades to further validate the absolute values of local erosion rates.

3. Results and discussion

3.1. Internal flow field characteristics

In numerical simulations, operating conditions were used with J of 0.3 and rotational speed of 3600 rpm. The selection of these conditions is based on theoretical analysis, with the aim of studying the pressure and velocity distribution of the RDTs flow field. The pressure and velocity contour plot of the RDTs flow field were obtained, which are consistent with the operating conditions described in Section 2.

The distribution characteristics of the flow field can be observed from Fig. 5. Firstly, the flow fields in the inlet and outlet sections exhibit stable pressure distribution and uniform velocity. In the inlet section, due to the low initial velocity of the fluid, the pressure distribution is relatively uniform, and the flow velocity is also relatively stable. In the outlet section, as the fluid enters the stable outlet area, there is little change in flow velocity and pressure, showing a certain stability. The stability of the inlet and outlet sections provides the foundation for the smooth operation of the entire flow field. However, in the transition section, the flow field exhibits significant fluctuations, with significant changes in pressure and velocity. From the simulation diagram, it can be seen that the pressure in the transition section shows decreasing trend as

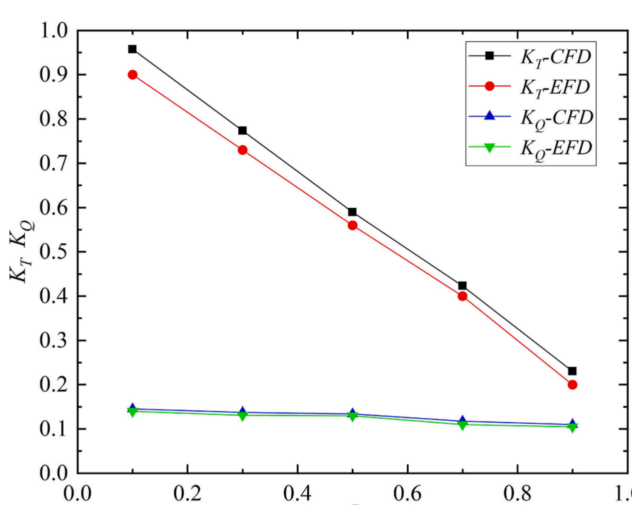

Fig. 4. Comparison of simulation and experimental results of hydrodynamic performance.

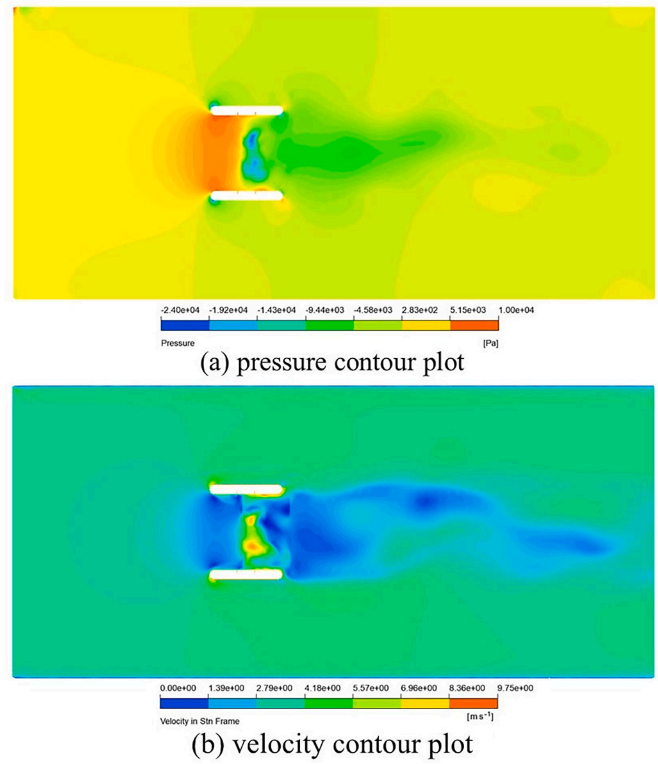

Fig. 5. RDTs pressure and velocity contour plot.

the flow velocity increases. This phenomenon indicates that there is a significant negative correlation between pressure and flow velocity when the fluid passes through the transition section. At the transition section, the flow state undergoes significant changes, with a decrease in pressure and an increase in flow velocity.

Further analysis reveals that there is still a negative pressure phenomenon in the transition section. The occurrence of negative pressure is due to the failure of fluid to be discharged in a timely manner when entering the RDTs rotation domain, resulting in significant pressure in the transition zone. When the fluid passes through the rotating region of the transition section, due to the effect of the rotating region, the fluid is subjected to different forces, and pressure is converted into kinetic energy. This process gradually increases the flow velocity, manifested as a significant increase in flow velocity at the transition section. This can be clearly observed from the trace diagram in Fig. 6. At the same time, the pressure in the transition zone is converted into kinetic energy, further promoting an increase in flow velocity. Due to these characteristics of the transition section, it can be predicted that severe erosion will occur in this area. Therefore, in the design and operation process, special attention must be paid to these areas to reduce possible damage.

To further quantify the flow-field variation in the transition section, several key parameters were extracted from the CFD results. The area-averaged turbulence intensity in the transition section reached 8.7%, which was much higher than that in the inlet section and outlet section, where the corresponding values were 1.9% and 2.6%, respectively. The vorticity magnitude also increased sharply in the transition section, with an area-averaged value of 2.34×10^2 and a maximum value of 5.28×10^2. By comparison, the area-averaged vorticity magnitudes in the inlet and outlet sections were only 3.6 and 6.4, respectively. In addition, the average pressure-gradient magnitude in the transition section was 2.86×10^5, approximately two orders of magnitude higher than that in the inlet section. The average velocity-gradient magnitude reached 3.74×10^2, indicating strong local acceleration and shear deformation when the flow entered the rotating domain. These quantitative results confirm that the transition section is a region with intensified

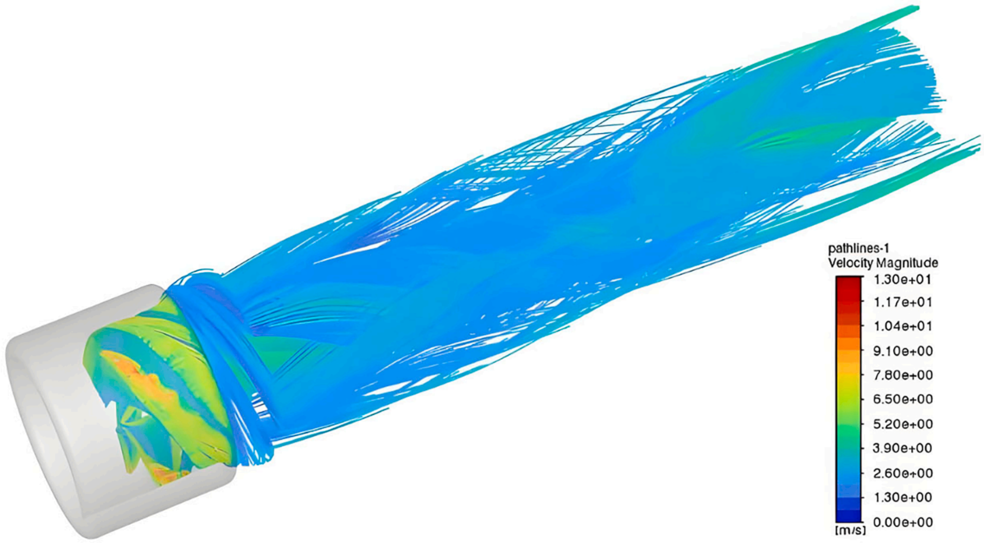

Fig. 6. Trace contour plot.

turbulence, vortex motion, pressure variation, and velocity shear. Therefore, sediment particles passing through this region are more likely to deviate from the mainstream flow and collide with the blade leading edge and rim-channel wall.

3.2. *Influence of particle size on erosion*

The coupling of Fluent and Rocky represents a typical application of integrating CFD with the DEM, widely used to analyze and simulate particle flow, particle impact, erosion, and other multi-physics coupling problems. Specifically, Fluent is a powerful CFD software for simulating airflow, liquid flow, heat transfer, and related fluid phenomena, whereas Rocky is a DEM software dedicated to modeling particle behavior, including collision, friction, and impact. In many engineering applications, the interaction between fluids and particles is highly complex. Traditional CFD simulations cannot independently model particle motion and impact, while DEM simulations alone are unable to account for fluid effects. By coupling these two tools, the interaction between fluid and particles can be described more accurately, thereby enabling comprehensive multi-physics analysis. In this study, DEM coupling is adopted for particle erosion analysis. Fig. 7 demonstrates the basic flow of the DEM coupling method between Fluent and Rocky.

In this section, Fluent and Rocky are employed with two-way coupling to investigate the particle-fluid interactions and erosion of the RDTs under different particle sizes. In two-way coupling, the interaction between particles and fluid is bidirectional. Fluent calculates the flow field (velocity, turbulence, pressure, etc.), and these flow characteristics are transferred to Rocky through boundary conditions. The motion of particles in the fluid is then influenced by the velocity field and turbulence, which subsequently affects particle collision, deposition, and transport. Conversely, in Rocky, the motion and interactions of particles generate forces that are fed back into Fluent, thereby altering the fluid velocity and pressure fields. This two-way coupling is realized through synchronized iterations in each time step, during which Fluent and Rocky exchange data until equilibrium is achieved. Such coupling enables more accurate simulation and analysis of fluid-particle

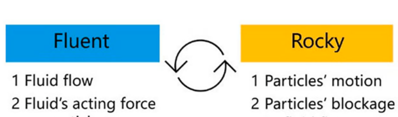

Fig. 7. DEM coupling method between Fluent and Rocky.

interactions. Through system coupling and two-way iteration, Fluent and Rocky can jointly resolve the complex interaction between fluid and particles, thereby addressing multi-physics problems in real engineering. This technique is widely applied in wind power, mineral processing, combustion, and other fields, offering significant benefits in improving design efficiency, reducing erosion losses, and optimizing particle flow. In the Fluent software, the fluid is set to be unsteady flow. In the DEM software module, a drag model and a lift model can be added. In the DEM software, set particles to appear uniformly at the inlet and apply an escape boundary condition at the outlet, the particle injection method adopts surface injection.

In present work, particles parameters are set as follow. Particles were defined as fine sediment particles, with diameters of 50 μm and 100 μm, density of 1500 kg/m^3, Poisson's ratio of 0.4, shear modulus of 21.3 MPa, and sphericity of 1.0. Particles with 50 μm were selected to represent fine suspended sediment with relatively strong flow-following capability, while particles with 100 μm were used to represent larger fine sediment particles with stronger inertia and higher impact potential. The Hertz-Mindlin model was employed with wall parameters identical to those of the particles, the restitution coefficient of 0.3, the static friction coefficient of 0.1 and the rolling friction coefficient of 0.1. When performing CFD-DEM coupling, the time step for the liquid phase should be 1 to 100 times that of the discrete phase. Therefore, the time step was set to be 1×10^{-4} s in the Fluent software and 1×10^{-6} s in the DEM. After every 100 steps of the DEM program, a data exchange is conducted with the CFD program. The user-defined function (UDF) file was used, and the coupling connection between Fluent and DEM is established. In this coupling strategy, the CFD time step of 1×10^{-4} was used to describe the transient evolution of the carrier-fluid flow field, whereas the DEM time step of 1×10^{-6} was adopted to resolve particle motion and particle–wall collisions. Therefore, one CFD time step contained 100 DEM sub-steps.

During each coupling exchange, the particle position, particle velocity, collision information and particle-induced momentum source terms calculated by Rocky were transferred to Fluent, while the updated fluid velocity, pressure, and turbulence quantities calculated by Fluent were transferred back to Rocky. This ensured that the particle motion was calculated with smaller time scale and that the fluid field was corrected by particle feedback once in each CFD time step. The coupled calculation was considered stable when the residuals of the fluid equations reached 10^{-4}, and the monitored thrust coefficient, torque coefficient, particle escape behavior, and particle–wall collision state no longer showed obvious temporal drift. Therefore, the selected coupling time-step ratio was considered capable of balancing particle-scale collision resolution and macroscopic flow-field update efficiency.

In high-velocity flow environments, RDTs blades are frequently subjected to impact from particles of varying diameters, such as sand, impurities or other solid matter. Surface erosion not only alters the aerodynamic performance of the blades but also reduces the efficiency and service life of the RDTs. Among the influencing factors, particles diameter is one of the most critical. In addition, blade geometry, particularly the diameter ratio (r/R), also have significant effect on erosion. The diameter ratio reflects the blade shape and flow distribution, influencing the velocity distribution, flow characteristics and fluid–particle interactions at the blade surface, thereby directly affecting particle impingement angles and erosion intensity. Therefore, analyzing the erosion performance of blades with different diameter ratios under different particle sizes can clarify the combined effects of these parameters on erosion resistance. In this work, the erosion caused by 100 μm and 50 μm particles is examined for different blade models, including variations in blade number and diameter ratio. Fig. 8 illustrates blade models with four, five, six, and seven blades, where the diameter ratio takes values of 0.9, 0.95, 1.0, 1.05, and 1.10. These configurations allow for investigating the combined influence of blade number and diameter ratio on erosion.

As observed, blade number directly affects the flow distribution and particles impingement angle. Fewer blades lead to flow concentration in the gaps between blades, forming strong vortices. When particles strike the blades, they concentrate in these regions, resulting in higher erosion intensity. In contrast, a larger number of blades produces more uniform flow distribution, reduces local vortices and weakens erosion intensity. Particles of 50 μm have relatively low kinetic energy, leading to weaker erosion intensity and more uniform erosion distribution. For four-blade, erosion is generally uniform and weak. Even at $r/R = 1.10$, where the leading edge is sharper, the low particle energy prevents significant concentrated erosion. As r/R increasing, erosion regions become even more uniform. For five-blade, erosion is nearly evenly distributed across the blade surface. Larger r/R values further reduce erosion strength, producing uniform, low-intensity erosion at $r/R = 1.10$. For six-blade, erosion distribution becomes more uniform with lower intensity, regardless of r/R. No concentrated erosion regions are observed, as the flow distribution and particle impingement angles diversify. For seven-blade, erosion is almost completely uniform and weak across the blade surface. Fluid distribution is most even, and particle impingement angles and intensities are well dispersed.

Particles of 100 μm exhibit significantly higher kinetic energy, producing stronger and more localized erosion. For four-blade, erosion is severe and concentrated, especially at small r/R values. At $r/R = 1.10$, the sharp leading edge combined with high flow velocity causes shallow-angle particle impacts, leading to severe erosion at the blade tips. At smaller r/R (e.g., 0.9), the blades are broader and the flow more evenly

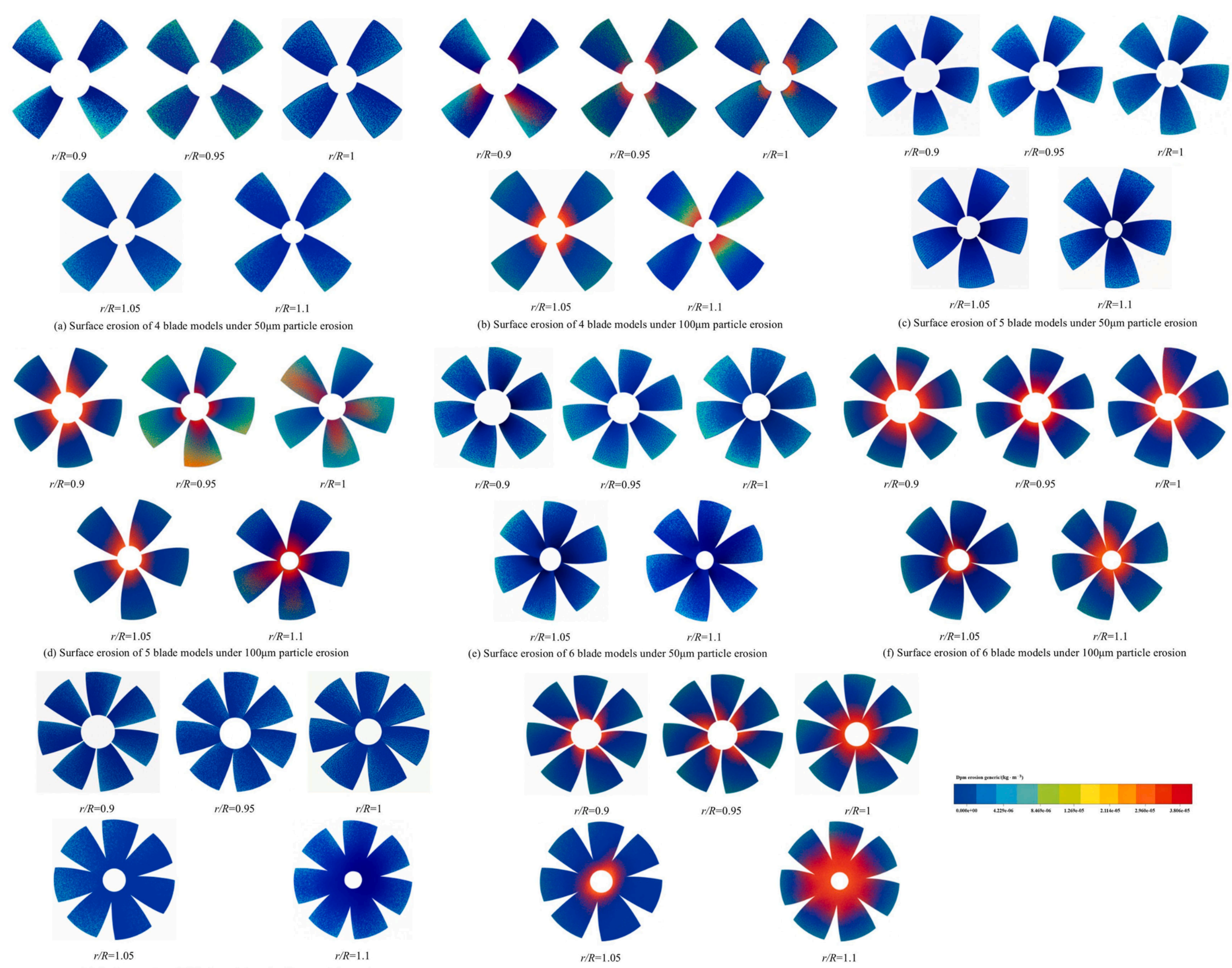

Fig. 8. Surface erosion of different blade models under 100/50 μm particle erosion.

distributed, reducing erosion intensity and spreading the erosion regions. For five-blade, the flow becomes more uniform, and erosion is more evenly distributed compared with the four-blade. Severe localized erosion disappears. At larger r/R, erosion is weaker and more dispersed, especially at the mid and trailing edges. For six-blade, erosion is further dispersed, particularly at $r/R = 1.05$ and 1.10, where erosion distribution is nearly uniform. Although smaller r/R values still concentrate erosion near the leading edge and blade root, the increased blade number disperses the flow, weakening localized erosion. For seven-blade, erosion is the most uniformly distributed. At $r/R = 1.10$, there are virtually no concentrated erosion regions. The fluid field is highly uniform, particle impingement angles are dispersed, and erosion intensity is consistently low across the blade surface.

Overall, larger particles result in stronger and more localized erosion, especially with fewer blades and smaller r/R values. Smaller particles, due to the lower kinetic energy, cause weaker and more evenly distributed erosion, with less sensitivity to blade number and r/R variations. Increasing the blade number and r/R value improves flow uniformity, reduces particle concentration effects, and mitigates erosion intensity, particularly for larger particles. Critical conditions for severe erosion are found in four-blade models with small r/R, where concentrated erosion occurs at the blade tips and roots. By contrast, larger r/R values promote more uniform erosion distribution with lower overall intensity. This analysis highlights the significant role of particle size in erosion behavior. Larger particles tend to generate severe localized erosion, whereas smaller particles produce weak, uniform erosion patterns. Increasing blade number and diameter ratio helps homogenize flow distribution, thereby reducing erosion, with particularly strong effects in mitigating erosion caused by large particles.

In the study of particle-induced erosion, it is essential to analyze both single size particles and polydisperse (mixed-size) particles, which is not only critical for engineering reliability but also for model realism and design rationality. Single size particle analysis offers controlled conditions that isolate the effect of particle size on erosion behavior. By using single size particles, it is possible to clarify the physical mechanisms, such as variations in particle kinetic energy, inertia and impact angle. Such analysis provides baseline references, allowing to identify the critical particle size that cause the strongest erosion and to establish fundamental models. For example, small particles tend to follow fluid streamlines, resulting in relatively uniform but weak erosion, while large particles have higher inertia and impact forces, leading to localized severe erosion. Through single size simulations, the particle size range with maximum erosion intensity can be determined, serving as guide for designing protective strategies. On the other hand, analyzing mixed particle sizes is indispensable, because in real operating conditions, particles are never single size. In natural and industrial environments, particle sizes typically follow statistical distribution.

Single size simulations can only approximate one class of particles and thus fail to represent the collective effects. In reality, surface damage is often the result of combined action, where large particles cause localized deep erosion and small ones produce surface abrasion and weaken protective coatings. The synergistic effect may even induce material fatigue or coating delamination. Therefore, relying solely on single size analysis may underestimate these compound effects. Mixed-size simulations provide more realistic representation and are more suitable for engineering predictions. In summary, single size particle analysis is indispensable for identifying fundamental trends, validating theories, and performing unit-scale experiments, whereas mixed-size analysis must be incorporated into practical engineering design, especially in complex sediment-laden particle systems. In this work, subsequent analysis focuses on the erosion behavior under mixed particles of 50-100 μm. For mixed particles model, the size distribution adopted follows Gaussian distribution. For the mixed-size case, the particle diameter followed truncated Gaussian distribution within 50–100 μm, with mean diameter of 75 μm and standard deviation of 8.33 μm.

Fig. 9 illustrates the erosion distribution of RDTs models subjected to mixed particles (50-100 μm) across diameter ratios of $r/R = 0.9$-1.10. Four-blade model: At $r/R = 0.9$-0.95, the most concentrated and severe erosion occurs, primarily along the leading edge and mid-blade regions. The leading edge, subject to high fluid velocity and steep impact angles, intensifies localized erosion. At $r/R = 1.0$, the severe erosion zone shrinks considerably, indicating that a rounder blade profile improves flow attachment and reduces particle focusing. At $r/R = 1.05$-1.10, erosion intensity remains low, with only minor traces at the blade tip. In the four-blade model, the improvement from increasing r/R is the most pronounced, especially beyond $r/R > 1$, where erosion distribution becomes more uniform. Five-blade model: For $r/R = 0.9$-1.0, severe erosion takes the form of a broad crescent-shaped zone, wide in coverage but low in concentration, resembling a “thin yet broad” erosion band. At $r/R = 1.05$-1.10, erosion becomes weaker and more scattered, as particle focusing is suppressed. Compared with the four-blade configuration, the five-blade model effectively disperses turbulence, reducing the extent of severe erosion. However, tip erosion persists at small r/R. Six-blade model: At $r/R = 0.90$-1.05, severe erosion forms a radiating pattern extending from the blade tips, shifting from the leading edge toward the root compared with the previous models. At $r/R = 1.10$, only the central blade region exhibits slight erosion, while the rest remains mildly affected, suggesting reduced turbulence excitation and earlier dissipation of particle energy. The six-blade configuration demonstrates strong erosion mitigation, especially at medium-to-high r/R, due to improved flow uniformity and earlier particle energy loss. Seven-blade model: At $r/R = 0.90$-1.0, despite the larger number of blades, severe erosion remains concentrated near the oblique leading edge under small r/R. At $r/R = 1.05$-1.10, erosion is predominantly mild, with only very small regions of severe erosion. This indicates that flow disturbance sufficiently suppresses particle clustering. At higher r/R values, the seven-blade configuration achieves the best erosion resistance, as particle energy is rapidly dispersed and local destructive effects remain minimal.

Compared with single size particle simulations, mixed-particle erosion exhibits the following characteristics: Broader erosion zones: Large, high-inertia particles concentrate in the high-speed core flow, producing severe erosion at the leading edge, while small particles are more susceptible to flow disturbances and penetrate the boundary layer, extending erosion into transition regions. Moderate overall intensity: The total erosion intensity lies between that caused by 50 μm and 100 μm particles. It is less localized than the 100 μm case and less uniform than the 50 μm case. Dispersed severe erosion: Severe erosion areas appear as scattered spots or strips, rather than concentrated patches, more closely resembling real-world erosion patterns observed in sediment-laden flows. Dual-scale erosion behavior: Large particles dominate impact-driven deep erosion, while small particles contribute to widespread surface abrasion. Their combined effect produces numerous small hotspots of severe erosion alongside extensive zones of mild erosion, which is valuable for identifying structural weak points. Thus, mixed-particle simulations more faithfully reflect real operating conditions, capturing both the impact-driven nature of large particles and the diffusive nature of small particles, and providing erosion patterns that align more closely with actual sediment erosion maps.

From Table 3, the variations in propulsion coefficient and torque coefficient under different blade numbers and particle diameters are observed. The data reveal distinct trends as the blade number increases. Increasing the number of blades generally leads to slight decrease in the propulsion coefficient. Although additional blades enhance the interaction with the fluid, they may also introduce greater turbulence, thereby reducing flow-through efficiency. Conversely, the torque coefficient typically increases with blade number, as more blades contribute to higher torque output, directly affecting the propeller's torque characteristics. Particles size also plays a significant role. Larger particles diameter affects the flow characteristics of the fluid, thereby influencing propeller performance. As particle size increases, the propulsion coefficient decreases, mainly due to the enhanced flow resistance caused by larger particles, which restricts fluid motion and reduces propulsive

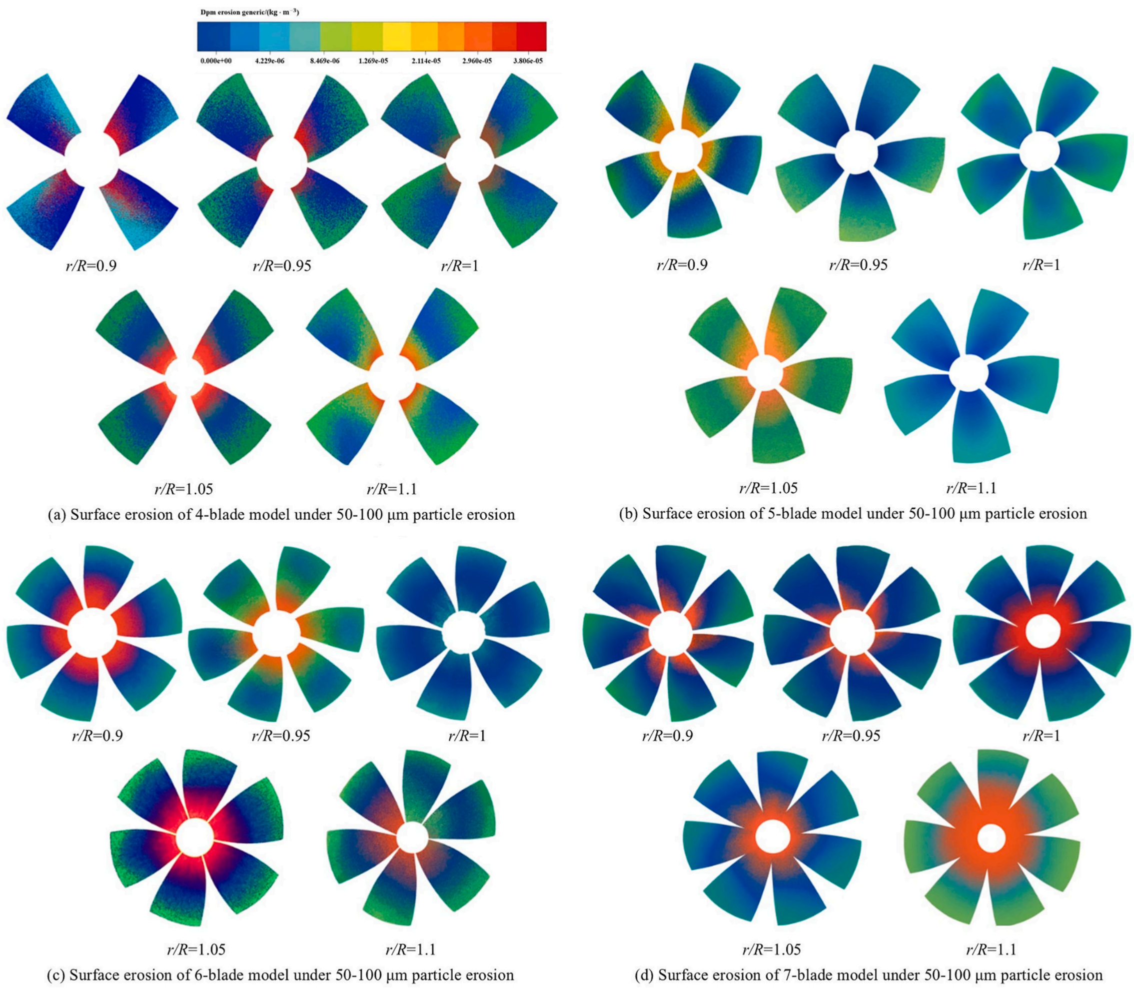

Fig. 9. Surface erosion of different blade models under 50-100 μm particle erosion.

Table 3
Thrust and torque coefficients under different blade models and particle parameters.

Blade Nos.	Particle diameter	K_T	K_Q
4	None	0.4084	0.1072
	50	0.3816	0.1014
	100	0.3591	0.0962
	50-100	0.3723	0.0983
5	None	0.3758	0.1054
	50	0.3570	0.1001
	100	0.3282	0.0946
	50-100	0.3364	0.0989
6	None	0.3720	0.1009
	50	0.3431	0.0987
	100	0.3248	0.0961
	50-100	0.3294	0.0979
7	None	0.3861	0.1130
	50	0.3601	0.1024
	100	0.3364	0.0973
	50-100	0.3408	0.0991

efficiency. At the same time, larger particles tend to increase the torque coefficient, as they effectively raise the density and viscosity of the working medium, demanding greater torque from the propeller.

Overall, when the blade number is relatively small, an increase in particle diameter results in a clear downward trend in propulsion coefficient, while the torque coefficient exhibits a more complex response. This complexity arises from the competing effects of increased flow resistance and torque demand associated with larger particles. For higher blade numbers, the influence of particle size becomes more pronounced: propulsion coefficient decreases more noticeably, while torque coefficient tends to rise, suggesting that a greater number of blades can better overcome the adverse effects of particles and sustain torque output. Mechanistically, increasing blade number generally enhances torque output but may slightly compromise propulsion efficiency. In contrast, larger particle sizes exert a dual effect by reducing propulsion efficiency and raising torque demand, leading to lower propulsion coefficients and higher torque coefficients.

To further clarify the effect of mixed particle sizes on hydrodynamic performance, the attenuation amplitudes of K_T and K_Q under 50, 100, and 50–100 μm particles were compared. Compared with the clean-water condition, the average reduction in K_T is 6.52% for 50 μm particles and 12.57% for 100 μm particles, while the mixed 50–100 μm particles produce an intermediate reduction of 10.63%. Similarly, the average reduction in K_Q is 5.50%, 9.79%, and 7.44% for 50 μm, 100 μm, and mixed-size particles, respectively. These results indicate that the performance degradation caused by mixed particles is located between the two mono-sized cases, but is closer to the 100 μm case. This suggests that larger particles play a more dominant role in hydrodynamic performance attenuation because of their stronger inertia and higher impact energy. To examine whether the mixed-size effect follows a simple superposition law, the K_T and K_Q values of the mixed-size particles were compared with the arithmetic average of the 50 μm and 100 μm cases.

The deviations of the mixed-size K_T from the mono-sized average are

0.53%, −1.81%, −1.36%, and −2.14% for the 4, 5, 6, and 7 blade models, respectively. The corresponding deviations of K_Q are −0.51%, 1.59%, 0.51%, and −0.75%. Therefore, from the perspective of global hydrodynamic coefficients, the performance attenuation under mixed particle sizes approximately follows the averaged trend of the mono-sized particle cases. However, the erosion distribution is not simple spatial superposition of the 50 μm and 100 μm erosion patterns. The larger particles mainly contribute to localized severe erosion near the blade leading edge and tip, whereas the smaller particles expand the mild abrasion region because of their stronger flow-following capability. Therefore, the mixed-size case represents coupled erosion behavior rather than purely linear superposition of the two mono-sized cases.

3.3. Influence of particle shape on erosion

The difference between non-spherical and spherical particles has significant effect on erosion behavior. Although traditional models often assume spherical particles for simplification, in practical applications particle shapes are usually complex and diverse, including irregular particles, elongated fiber-like particles, and flat particles. Non-spherical particles may exhibit various geometrical structures such as elongated, flattened or irregular forms. These morphological difference directly affects the motion in fluids and the collision behavior with surfaces. Some common particle shapes are shown in Fig. 10. In contrast, spherical particles are generally uniform geometry, which makes the flow behavior more symmetrical and the motion trajectories and force analysis relatively straightforward. When colliding with surfaces, non-spherical particles, due to the uneven geometry, tend to larger contact areas. This results in increased frictional and shear forces at the impact interface, thereby intensifying erosion effects. Spherical particles, on the other hand, usually make contact with smaller areas of the surface, leading to more distributed impact force and relatively uniform erosion process. The influence of non-spherical particles on erosion is therefore more pronounced, as the complex shapes cause greater impact forces and stronger localized damage. Since particles morphology directly affects the distribution, intensity and mechanism of erosion, neglecting non-spherical particles in design and simulations may underestimate erosion risks. For this reason, engineering design must consider range of particle shapes.

Based on this consideration, the present study compares the erosion behaviors of spherical and barley-shaped particles. By examining both 100 μm and 50 μm particles, while also accounting for variations in blade number and diameter ratio (r/R), the influence of these parameters on erosion patterns is further investigated, spherical particles were adopted as the ideal reference shape, whereas Barley-shaped particles were selected to approximate non-spherical natural sediment particles, and the nominal diameter refers to the equivalent-volume diameter.

As shown in Fig. 11, the blade surfaces exhibit pronounced erosion when subjected to 100 μm particles. Larger particles, having higher inertia, are less influenced by fluid motion and therefore exert stronger impact forces. When these particles strike the blade surface, the impacts are concentrated along the blade edges, forming localized regions of severe erosion. In the RDTs model, such large particles, due to the high kinetic energy, tend to cause deep and localized erosion, particularly along the blade leading edge. This occurs because the leading edge, located in high-speed flow zones, is frequently subjected to particle collisions, and larger particles with strong inertia and smaller impact angles intensify the local damage. Consequently, 100 μm particles induce strong impact forces capable of stripping surface material and causing localized structural damage. The leading edge and curved sections of the blade are especially vulnerable due to repeated collisions, leading to severe erosion. By comparison, 50 μm particles have lower inertia and therefore generate weaker impacts. Erosion caused by 50 μm particles is more diffuse, generally manifesting as mild surface wear. Despite the weaker impact force, 50 μm particles still contribute to blade surface wear, especially in the central blade regions. Unlike larger particles, smaller particles exhibit more uniform distribution of impact forces, leading to smoother erosion patterns. However, over extended operation, the continuous bombardment of small particles may gradually degrade blade surfaces, posing long-term risks to performance and durability. Overall, larger particles tend to produce highly localized and severe erosion, stripping material from the blade and leaving pits or grooves, while smaller particles result in more uniform but cumulative wear over time.

When the blade number is small, each blade is subjected to higher impact forces, leading to concentrated erosion, especially along the leading edge. With fewer blades, particles in the flow are more likely to strike localized blade regions, resulting in pronounced local damage. By contrast, when the blade number is larger, the impact forces are more evenly distributed, producing smoother erosion profile. In the erosion maps, higher blade counts correspond to weaker and more evenly spread erosion. Thus, fewer blades exacerbate localized erosion, whereas more

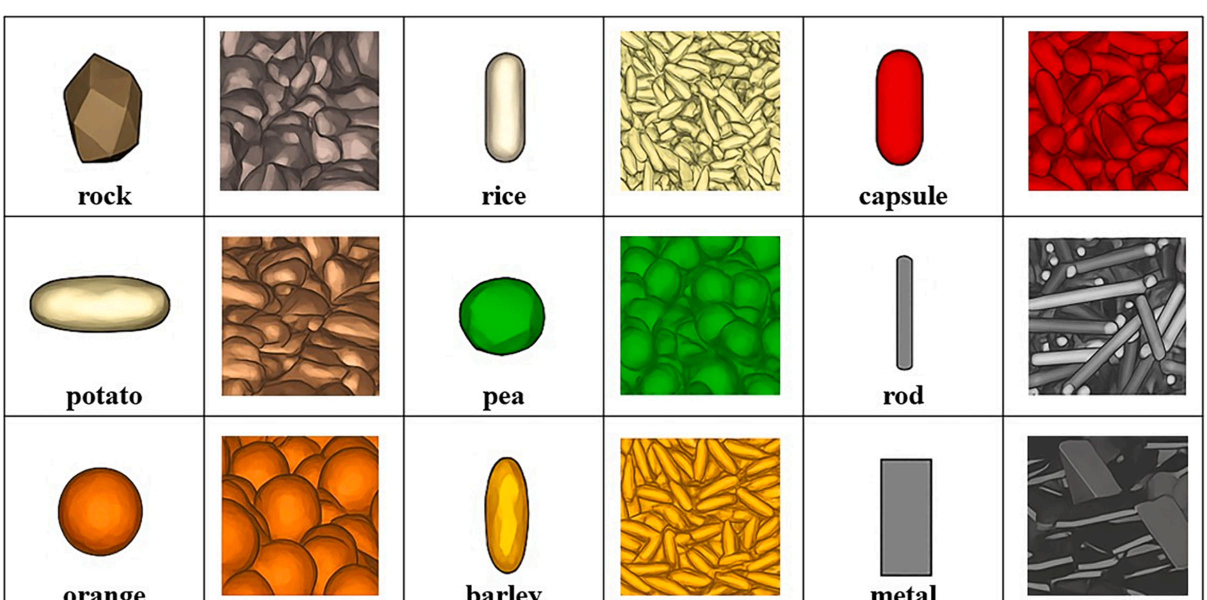

Fig. 10. Different particle shapes available in the Rocky library.

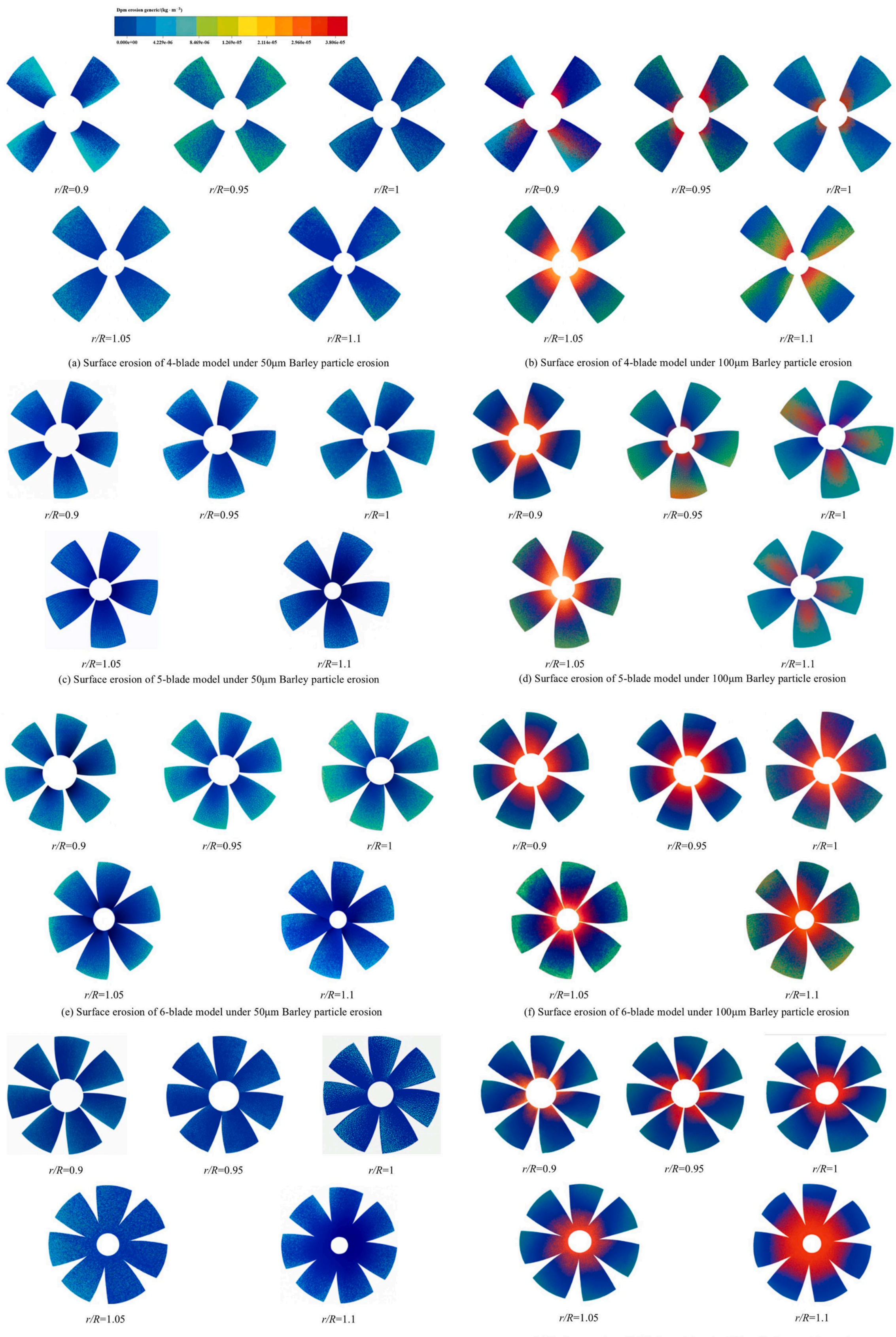

Fig. 11. Surface erosion of different blade models under 50/100 μm Barley particle erosion.

blades mitigate concentration and distribute erosion more uniformly. The diameter ratio (r/R) also plays a key role. At smaller r/R values, blades generally feature larger root curvature, causing particles to strike at smaller angles and concentrate erosion near the leading edge. This leads to large, intense erosion zones. At larger r/R values, blade shapes are straighter, flow angles are smoother, and erosion becomes more evenly distributed, with reduced localized intensity. As a result, the overall erosion level decreases, and severe erosion regions are less evident. Regular spherical particles usually produce more uniform erosion due to the small contact area with blade surfaces and more distributed impact forces. The impact behavior is relatively straightforward, making them suitable for use in theoretical models. However, with irregular particles, the influence of morphology, edges and size becomes pronounced. Particles with sharp edges may deliver multiple impacts upon collision, intensifying localized erosion. The complex geometries lead to asymmetric impacts, producing stronger localized damage and making erosion prediction more challenging. Compared with spherical particles, irregular particles generally cause more concentrated erosion with higher impact intensity, consistent with the asymmetry and shape complexity.

In summary, large particles tend to cause more severe and localized erosion, particularly along leading edges and curved sections, while small particles produce more uniform erosion but may accumulate to cause long-term wear. Blade number and diameter ratio (r/R) strongly influence erosion distribution, with fewer blades leading to concentrated erosion and larger r/R values reducing overall erosion intensity. Finally, particle shape is a decisive factor: irregular particles cause more complex and severe localized erosion compared to regular spheres, making their consideration essential in realistic engineering assessments.

Fig. 12 analyzes the maximum erosion rate under varying blade numbers, particle diameters and particle shapes. These results illustrate the influence of particle diameter on blade erosion rates, while also revealing how erosion trends differ significantly across blade numbers and particle morphologies. The results show that both blade number and particle shape exert marked influence on the maximum erosion rate. With fewer blades, the maximum erosion rate is generally higher, particularly at larger particle diameters. This arises because fewer blades lead to higher impact frequency per blade, intensifying localized collisions and thereby producing higher erosion rates. Conversely, with a larger number of blades, the maximum erosion rate decreases, especially at smaller particle diameters. In this case, particle impacts are more evenly distributed, reducing the number of collisions per blade,

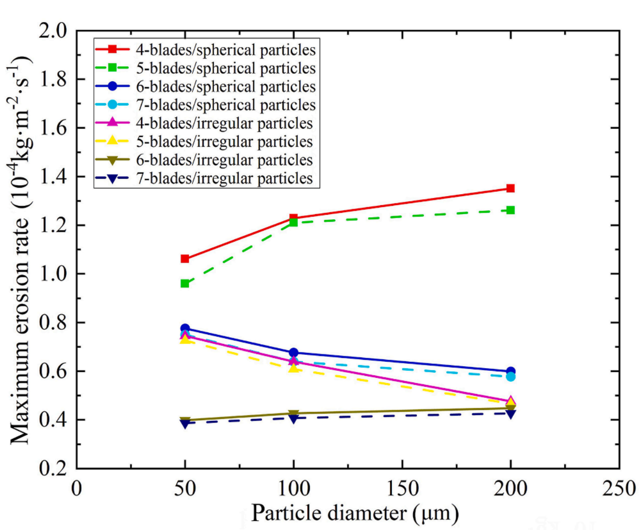

Fig. 12. Comparison of maximum erosion rates under different models and particle parameters.

which lowers localized impact intensity and thus diminishes the overall erosion rate.

With respect to particle shape, regular particles consistently yield lower erosion rates across the diameter range. The uniform geometry produces smoother contact with blade surfaces, resulting in more evenly distributed impact forces and therefore weaker localized erosion. In contrast, irregular particles generally produce higher erosion rates. The non-uniform geometries create uneven impact points, concentrating collision forces in certain regions and causing more severe localized erosion. For the same particle diameter, irregular particles generate significantly higher erosion rates than regular ones. The effect of particle diameter is also evident. At larger particle diameters, erosion rates are generally high. This is especially pronounced with fewer blades, where particle impacts are stronger and localized erosion more severe. For regular particles at these diameters, erosion forces remain relatively uniform, but erosion rates are still elevated due to persistent surface bombardment. Irregular particles, however, exhibit stronger erosion effects in this range, with impact forces concentrated unevenly and erosion rates significantly higher. As particle diameter decreases, erosion rates show general decline. Smaller particles, due to the weaker inertia, are less easily entrained by the flow and thus make fewer contacts with blade surfaces. This reduces both the frequency and the intensity of impacts. Furthermore, smaller particles are less likely to undergo repeated collisions with the same surface regions, thereby lowering localized erosion. As a result, small particles especially regular ones exhibit distinct downward trend in erosion rate at smaller diameters.

From the overall trends, several key observations emerge. First, erosion rates decline with increasing blade number, reflecting the effect of impact distribution. More blades disperse particle impacts across wider surface area, thereby reducing the local intensity on each blade and lowering the global erosion rate. Second, particle shape has pronounced effect: irregular particles produce higher erosion rates, especially at small diameters, due to uneven contact and concentrated impact forces, whereas regular particles exhibit more uniform and less damaging erosion behavior. Third, particle diameter influences erosion in non-linear fashion. Large particles produce higher erosion rates, particularly with fewer blades, but erosion decreases progressively with decreasing diameter. This decline is more pronounced for regular particles than for irregular ones. In summary, increasing blade number effectively reduces localized erosion rates, particularly under large-particle conditions, making multi-blade configurations advantageous for erosion mitigation. Particle shape plays a decisive role, with irregular particles causing significantly higher erosion rates than regular ones, underscoring the importance of accounting for particle morphology in design. Particle size also strongly influences erosion: larger particles induce severe localized wear, while smaller particles lead to progressively lower erosion rates, with this effect most evident in the case of regular particles.

As shown in Table 4, increasing particle size, irregular particle morphology and higher particle mass flow rate significantly increase both the maximum and area-averaged erosion rates, while the lower coefficient of variation in the 7 blades cases indicates improved erosion distribution uniformity. Representative statistical parameters were further extracted to quantify erosion severity and distribution uniformity. For the four-blade spherical-particle case, increasing particle diameter from 50 μm to 100 μm increased the maximum erosion rate from 1.72×10^{-7} to 4.85×10^{-7}, and the coefficient of variation from 0.91 to 1.30, indicating stronger and more localized erosion. The mixed 50–100 μm particles showed intermediate maximum and average erosion rates of 3.62×10^{-7} and 0.74×10^{-7}, respectively. For 100 μm particles, changing the particle shape from spherical to Barley increased the maximum erosion rate from 4.85×10^{-7} to 6.02×10^{-7}, confirming that irregular particles enhance localized erosion. Moreover, increasing the particle mass flow rate from 0.05 kg/s to 0.10 kg/s increased the average erosion rate from 0.93×10^{-7} to 1.68×10^{-7} for the four-blade

Table 4
Representative statistical parameters of erosion-rate distribution.

Case	Blade Nos.	Particle condition	Mass flow rate (kg/s)	Max. erosion rate	Ave. erosion rate	Coef.
Particle size	4	50 μm spherical	-	1.72	0.43	0.91
Particle size	4	100 μm spherical	-	4.85	0.91	1.30
Mixed-size	4	50–100 μm spherical	-	3.62	0.74	1.11
Particle shape	4	100 μm Barley	-	6.02	1.17	1.32
Mass flow rate	4	50–100 μm Barley	0.05	4.70	0.93	1.16
Mass flow rate	4	50–100 μm Barley	0.10	7.88	1.68	1.15
Blade number	7	100 μm spherical	-	3.05	0.66	0.88
Blade number	7	100 μm Barley	-	3.92	0.80	1.06

mixed Barley-particle case. These statistical results support the contour-based observation that larger particles, irregular particle morphology, and higher particle loading intensify erosion, whereas increasing blade number improves erosion distribution uniformity.

As listed in Table 5, under the same blade number and particle diameter, Barley-shaped particles lead to lower K_T and K_Q than spherical particles. Based on the present data, the reduction in K_T caused by Barley-shaped particles ranges from 2.98% to 4.34%, with an average reduction of 3.57%. The reduction in K_Q ranges from 0.42% to 2.73%, with an average reduction of 1.38%. This indicates that non-spherical particles have more pronounced influence on thrust reduction than on torque reduction. Compared with spherical particles, Barley-shaped particles have more complex orientation-dependent motion and particle-wall contact behavior, which may enhance local particle–fluid interaction and near-wall disturbance. In addition, the non-spherical morphology is more likely to produce cutting and sliding erosion on the blade surface, increasing surface roughness and weakening the effective blade loading. Therefore, the decrease in K_T under Barley-shaped particles can be mainly attributed to the combined effects of non-spherical particle disturbance and stronger erosion-induced surface deterioration.

In summary, under the same blade number and particle diameter, Barley-shaped particles systematically decrease both K_T and K_Q. The underlying physical mechanism lies in the enhanced mixing and secondary flow losses, together with stronger cutting-type erosion, which aggravate blade surface roughness and separation tendency, thereby reducing lift and efficiency. This adverse effect becomes more pronounced as particle diameter increases.

The volume-averaged turbulent kinetic energy (TKE) and the secondary flow intensity coefficient (C_{sf}) are defined according to the following equations:

$$TKE = \frac{1}{V}\int_V k dV \tag{19}$$

Table 5
Thrust and torque coefficients under different particle shapes.

Blade Nos.	Particle diameter	Particle shape	*TKE*	C_{sf}	K_T	K_Q
4	100	Spherical	0.0420	0.0803	0.3591	0.0962
		Barley	0.0475	0.0874	0.3435	0.0958
	50	Spherical	0.0381	0.0756	0.3816	0.1014
		Barley	0.0416	0.0802	0.3694	0.1002
5	100	Spherical	0.0414	0.0791	0.3282	0.0946
		Barley	0.0451	0.0854	0.3161	0.0934
	50	Spherical	0.0372	0.0743	0.3570	0.1001
		Barley	0.0411	0.0806	0.3438	0.0985
6	100	Spherical	0.0403	0.0781	0.3284	0.0961
		Barley	0.0452	0.0855	0.3186	0.0949
	50	Spherical	0.0360	0.0736	0.3431	0.0987
		Barley	0.0396	0.0784	0.3318	0.0978
7	100	Spherical	0.0387	0.0741	0.3364	0.0973
		Barley	0.0439	0.0756	0.3219	0.0957
	50	Spherical	0.0351	0.0729	0.3601	0.1024
		Barley	0.0382	0.0761	0.3492	0.0996

$$C_{sf} = \frac{\frac{1}{A}\int_A \sqrt{{U_r}^2 + {U_\theta}^2} dA}{\frac{1}{A}\int_A U_z dA} \tag{20}$$

Where V is the volume of the impeller region, A is the cross-sectional area at the impeller outlet. These two parameters are used to quantitatively characterize the turbulence enhancement and secondary flow losses induced by particle shape.

To substantiate the mechanism by which barley-shaped particles reduce K_T, the volume-averaged *TKE* and the C_{sf} at the impeller outlet plane were extracted from the CFD-DEM results. As shown in Table 5, barley-shaped particles consistently produce higher *TKE* and C_{sf} values than spherical particles across all blade numbers and particle diameters. For example, at the four-blade, 100 μm condition, *TKE* increases from 0.0420 m^2/s^2 to 0.0475 m^2/s^2, while C_{sf} rises from 0.080 to 0.087. Similar trends are observed for all other cases, with *TKE* enhancements of 9–13% and C_{sf} enhancements of 6–9%. These quantitative data confirm that non-spherical morphology intensifies turbulent fluctuations and secondary motion, leading to higher dissipation and degraded momentum transfer, which directly causes the 3–4% reduction in K_T observed in the table.

3.4. *Effect of particle mass flow rate on erosion*

The particle mass flow rate is a critical factor in RDTs under particle erosion conditions, as it directly affects the operating state, loading characteristics and performance of the propeller in sediment-laden environments. A larger mass flow rate indicates that a greater number of particles impact the propeller per unit time, thereby intensifying the erosion severity. RDTs are commonly employed in navigation and pumping applications, where sediment particle impacts are often unavoidable. The performance of the propeller in practical working environments can be analyzed, and improvements can be made to blade geometry, dimensions, and material selection in order to enhance adaptability and stability under complex sediment conditions. The particle mass flow rate can influence erosion intensity, material selection, performance variation, design optimization, and maintenance strategies. The potential benefit may extend service life and provide valuable guidance for design and operational practices in engineering applications.

To further analyze the influence of particle mass flow rate on the wear characteristics of RDTs, this section considers the average wear rate of propellers under two different flow rates, 0.05 kg/s and 0.10 kg/s. These mass flow rates correspond to particle volume concentrations of approximately 0.0134% and 0.0268%, respectively, indicating that both cases remain within the dilute sediment-laden flow regime, with Barley-shaped particles of 50–100 μm, as illustrated in Fig. 13. It can be observed that the leading edge of the blade, being the first region to encounter the flow field, experiences direct particle impacts due to the relatively high velocity in this area. Under the low-flow condition, the particle kinetic energy is comparatively small, and the local impact force is uneven, causing erosion hotspots to concentrate in specific zones of the blade leading edge (near the suction side). With an increase in mass flow rate, the turbulence intensity rises, leading to more violent impacts

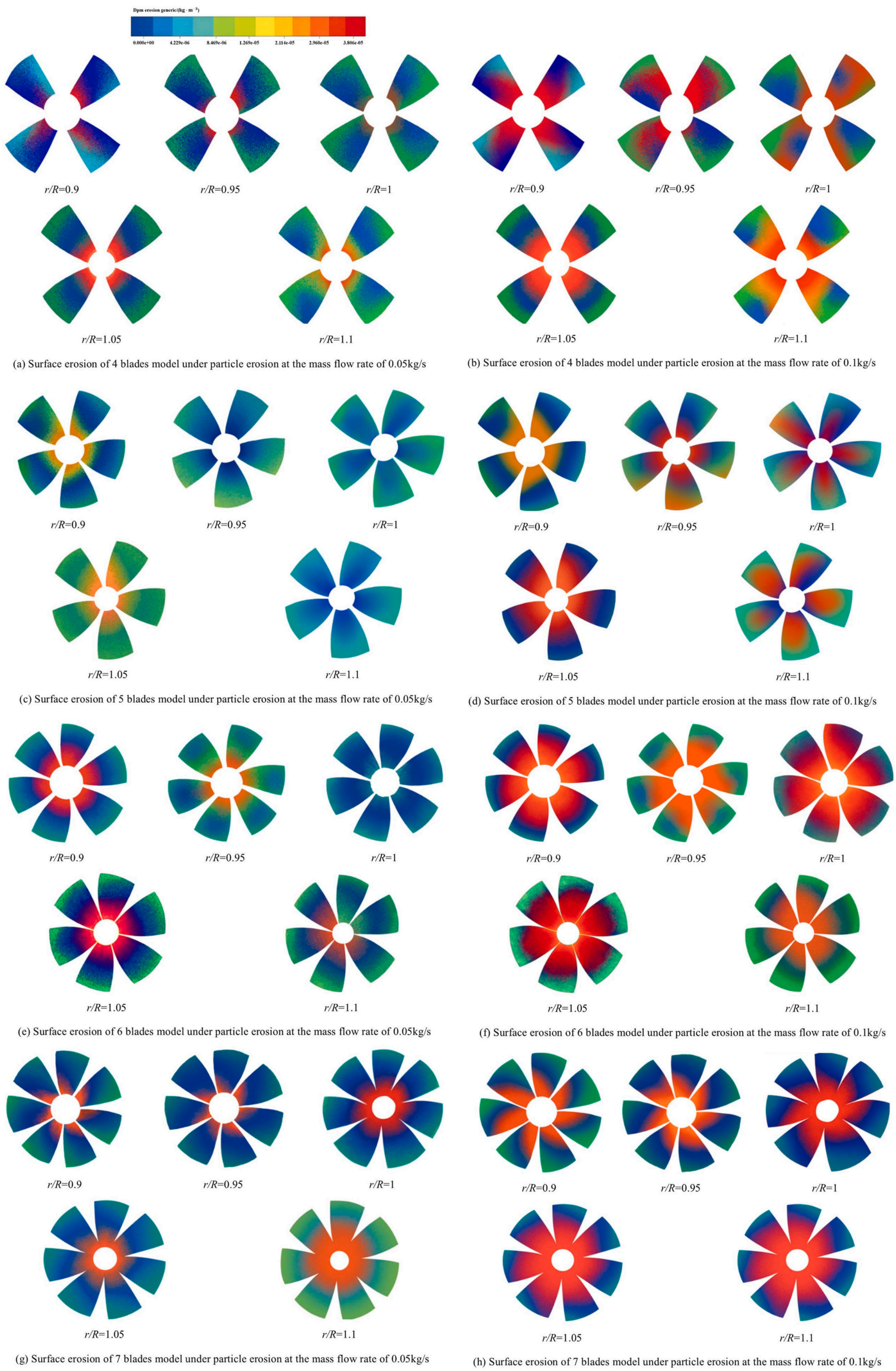

Fig. 13. Surface erosion of different blade models under particle erosion at different mass flow rates.

of particles on the blade surface. The erosion extends from small localized region to the entire band of the leading edge, and even begins spreading toward the mid-blade section. The increase in erosion at the blade tip is strongly correlated with the mass flow rate, particularly under the high-flow condition, where the flow becomes more unstable and results in intensified particle impacts at the tip. Regardless of the flow rate, the suction side consistently serves as the critical erosion-prone area, owing to relatively large velocity gradient and denser streamlines, which increase particle impact energy.

As the mass flow rate rises, fluid acceleration effects become more significant, and the forces exerted on particles grow larger, leading to stronger impact forces. Consequently, the erosion band gradually extends toward the pressure side, especially in the 6- and 7-blade models, where notable erosion also emerges on the pressure surface. An increase in blade number reduces the flow area per blade, thereby distributing the fluid loading across more blades. With additional blades, the impact force on each blade decreases, which alleviates erosion intensity. At smaller mass flow rates, models with fewer blades exhibit heavier loading per blade, resulting in the formation of localized high-intensity erosion spots. With more blades, the local impact force per blade decreases, and erosion regions expand while becoming more uniform. Under the condition of 0.05 kg/s, the particle impact energy remains relatively low, so erosion is primarily localized. The main features include erosion hotspots and small-scale concentrated zones. In models with fewer blades, where the overall flow is limited, particle distribution tends to be uneven, producing high-erosion regions at the leading edge, particularly near the outer radius of the blade. At the higher mass flow rate of 0.10 kg/s, the intensified turbulence elevates particle kinetic energy, leading to stronger impact forces and broader erosion bands. Under this condition, the flow is more unstable, and particle distribution is more uniform, causing the erosion range to expand significantly. Not only is the leading edge affected, but other regions of the blade, such as the mid-span and root, also begin to experience erosion, and the affected area becomes markedly larger.

In summary, with increasing mass flow rate, particle kinetic energy is enhanced, which results in stronger erosion intensity and the expansion of erosion regions from localized hotspots to the entire blade surface, with particularly significant increases observed at the blade tip.

Based on the simulation results, particles size was identified as the most sensitive factor affecting erosion intensity and hydrodynamic performance degradation. Compared with the clean-water condition, the average K_T attenuation was 6.52%, 12.57%, and 10.63% for 50 μm, 100 μm, and 50–100 μm mixed particles, respectively. The corresponding average K_Q attenuation was 5.50%, 9.79%, and 7.44%. Particle shape also had a significant influence: compared with spherical particles, Barley-shaped particles further reduced K_T and K_Q by 3.57% and 1.38% on average, respectively. The erosion contours further show that structural parameters mainly regulate erosion distribution. Fewer blades and smaller r/R values intensify local erosion concentration, whereas increasing blade number and r/R weakens particle focusing and improves erosion uniformity. Therefore, particles size and shape dominate the erosion intensity, while blade number and r/ R modulate the interaction between particle impacts and blade-surface erosion.

4. Conclusion

This study provides brief introduction to the RDTs, the mechanisms of particle erosion and the research methods for hydrodynamic performance. A numerical model for RDTs under sediment particle erosion conditions was established and the erosion and performance prediction were conducted. The main conclusions are as follows:

(1) The simulation results indicate that larger particles, due to the stronger inertia, are more likely to induce concentrated erosion at the blade leading edge and in high-velocity regions, thereby causing localized deep wear. In contrast, smaller particles exhibit better flow-following behavior, resulting in more uniformly distributed but lower-intensity erosion pattern, which manifests as gradual long-term damage mode. Mixed particle sizes, however, demonstrate combined effect: localized severe erosion caused by large particles and widespread uniform wear induced by small particles, thereby resembling actual operating conditions more closely.

(2) The results reveal that when the blade number is relatively small, the flow distribution becomes non-uniform, with pronounced local vortex effects that readily induce concentrated erosion at the blade tip and root. As the blade number increases, the uniformity of the flow field is significantly improved, the particle impact distribution becomes more dispersed, and the regions of severe erosion are markedly reduced. This indicates that increasing the blade number can, to a certain extent, decrease the sensitivity to erosion.

(3) Compared with the single particle size, the erosion distribution under mixed particle-size conditions is more complex: large particles dominate localized deep impacts, while small particles broaden the abrasion range, resulting in wider but moderately intense erosion region. This combined pattern of "point-like concentration and surface-wide distribution" exhibits a high degree of consistency with actual sediment-laden and particle-laden flow conditions.

(4) The results demonstrate that regular spherical particles produce relatively uniform erosion on the blade surface, with comparatively lower wear rate. In contrast, irregular particles (such as Barley-type) possess pronounced edges and larger contact areas with the blade surface, making them more prone to forming highly concentrated and destructive erosion regions. This effect is particularly evident under the action of larger particles, where irregular particles significantly aggravate damage at the leading edge and curved sections.

(5) The results indicate that with increasing particle size, the thrust coefficient exhibits declining trend, reflecting a reduction in propulsion efficiency, while the torque coefficient generally rises, indicating an increase in propeller loading in particle-laden flows. This effect is more pronounced when the blade number is relatively small, whereas a greater number of blades helps to distribute particle impacts, thereby mitigating the extent of efficiency loss and torque rise. This pattern reveals the coupled influence of blade number and particle size on propulsion performance degradation, providing an optimization direction for propeller design.

(6) Based on the simulation cases, particles size is found to be the most sensitive factor affecting erosion intensity and hydrodynamic performance attenuation, followed by particle shape and particle mass flow rate. Structural parameters, including blade number and r/R, mainly influence the spatial distribution of erosion and can weaken the localized erosion caused by large or irregular particles.

(7) Due to the limitation of the current laboratory facilities, experimental validation of hydrodynamic coefficients and erosion predictions from the CFD-DEM model has not been performed. In future work, a sediment-laden thruster experiment covering a range of particle sizes, concentrations and flow velocities will be conducted to quantitatively validate and refine the model.

CRediT authorship contribution statement

Nan Wang: Writing – original draft, Validation, Software, Investigation, Data curation. **Zhentao Wang:** Writing – review & editing, Supervision, Software, Resources, Project administration, Methodology, Funding acquisition, Formal analysis, Conceptualization. **Bin Li:** Supervision, Software, Methodology, Funding acquisition, Formal analysis, Conceptualization. **Qingming Dong:** Supervision, Software, Resources, Funding acquisition, Data curation. **Junfeng Wang:** Supervision, Conceptualization. **Jiyuan Tu:** Writing – review & editing, Supervision, Project administration, Methodology, Conceptualization.

Declaration of competing interest

The authors declare that they have no known competing financial interests or personal relationships that could have appeared to influence the work reported in this paper.

Acknowledgments

This work was supported by the National Natural Science Foundation of China (grant No. 52076105; 52206199), and Key Laboratory of Advanced Reactor Engineering and Safety, Ministry of Education (grant No. ARES-2025-01).

References

Adachi, M., Shirode, K., Hatano, N., Tanaka, K., & Kanamori, H. (2024). Climbing characteristics of millimeter particles in granular vibration pumping system. *Powder Technology, 447*, Article 120200.

Cao, Q. M., Hong, F. W., Tang, D. H., Hu, F. L., & Lu, L. Z. (2012). Prediction of loading distribution and hydrodynamic measurements for propeller blades in a rim driven thruster. *Journal of Hydrodynamics, 24*(1), 50–57.

Cao, Q. M., Zhao, W. F., Tang, D. H., & Hong, F. W. (2015). Effect of gap flow on the torque for blades in a rim driven thruster without axial pressure gradient. *Procedia Engineering, 126*, 680–685.

Chen, H., Fan, M., Su, W., Guo, Y., & Huang, Y. (2021). Effects of particle erosion on the submersible pump in an ultra-high voltage transformer. *Energy Reports, 7*, 7072–7081.

Chen, Y., Wang, L., & Hua, H. X. (2017). Longitudinal vibration and unsteady thrust transmission of the rim driven thruster induced by ingested turbulence. *Ocean Engineering, 131*, 149–161.

Cheng, W., Fan, H., Cheng, W., & Shao, C. (2024). Investigation on wear induced by solid-liquid two-phase flow in a centrifugal pump based on EDEM-fluent coupling method. *Flow Measurement and Instrumentation, 96*, Article 102542.

Gao, C., Xu, G., Shen, F., Du, W., Xu, P., Zhang, Q., & Lu, P. (2025). Numerical simulation on liquid-solid two-phase erosion characteristics of pipe bends with different bend angles. *Chemical Engineering Research and Design, 216*, 390–413.

Hirt, C. W., & Nichols, B. D. (1981). Volume of fluid (VOF) method for the dynamics of free boundaries. *Journal of Computational Physics, 39*(1), 201–225.

Inoue, T., Hirotsugu, Y., Kashiwada, J., & Nihei, Y. (2025). Interaction between horseshoe vortex structure and sediment transport around a river rectangular pier using a solid-liquid two-phase turbulent LES model. *International Journal of Multiphase Flow, 186*, Article 105153.

Jing, J., Chen, Z., Wang, G., & Tang, K. (2024). Study on the law and mechanism of particle migration in high pressure pumping pipeline. *Chemical Engineering Research and Design, 212*, 81–96.

Karim, M. M., & Ahmmed, M. S. (2012). Numerical study of periodic cavitating flow around NACA0012 hydrofoil. *Ocean Engineering, 55*, 81–87.

Ko, Y. H., Chen, J. S., Hsiao, Y. C., Cantor, H. F. P., Chen, W. J., Hung, J. W., Haung, H. C., Huang, T. Y., & Su, T. C. (2025). Effects of particle shape, breakage properties, and operating parameters on blast furnace raceway size through CFD-DEM simulations and cold-model experiments. *Powder Technology, 458*, Article 120952.

Lai, S. H. (2006). *Design optimisation of a slotless brushless permanent magnet DC motor with helically-wound laminations for underwater rim-driven thrusters*. Doctoral dissertation. University of Southampton.

Li, M. M., Hong, Y., Zhang, H. L., Wang, R. G., & He, X. D. (2025). The numerical research on cavitation performance of the composite propeller under uniform and non-uniform inflow. *Ocean Engineering, 322*, Article 120399.

Li, P., Sun, C., Yao, H. D., Wang, Z., Wang, C., & Weng, K. (2023). The effects of domain division types on the performance prediction of a rim-driven thruster. *Ocean Engineering, 287*, Article 115809.

Nie, Y., Ouyang, W., Zhang, Z., Li, G., & Zheng, R. (2023). Multi-parameter optimization analysis of hydrodynamic performance for rim-driven thruster. *Energies, 16*(2), 891.

Peng, W., Cao, X., Ma, L., Wang, P., Bian, J., & Lin, C. (2023). Sand erosion prediction models for two-phase flow pipe bends and their application in gas-liquid-solid multiphase flow erosion. *Powder Technology, 421*, Article 118421.

Pu, W., Ji, L., Li, W., Shi, W., Yang, Y., Li, H., & Zhang, X. (2024). Experimental study of solid-liquid two-phase flow field in a centrifugal pump volute under multiple working conditions. *Flow Measurement and Instrumentation, 100*, Article 102739.

Schmunk, C., Dogan, M., & Altun, S. (2023). Predicting propeller jet scour in silty and sandy marine environments. *Ocean Engineering, 286*, Article 115558.

Shih, T. H., Liou, W. W., Shabbir, A., Yang, Z., & Zhu, J. (1995). A new k-ϵ eddy viscosity model for high reynolds number turbulent flows. *Computers & Fluids, 24*(3), 227–238.

Sommerfeld, M., & Taborda, M. A. (2024). Collision rates of small solid particles with rigid spherical and spheroidal bubbles in laminar flow. *Experimental and Computational Multiphase Flow, 6*(4), 365–386.

Suryanarayana, C., Satyanarayana, B., Ramji, K., & Rao, M. N. (2010). Cavitation studies on axi-symmetric underwater body with pumpjet propulsor in cavitation tunnel. *International Journal of Naval Architecture and Ocean Engineering, 2*(4), 185–194.

Vieira, C. B., de Ghelin, O. F., Goffaux, C., Nicolle, T., & Dupont, V. (2024). Numerical challenges of CFD simulations of two-phase injectors working in the direct contact condensation mode. *Experimental and Computational Multiphase Flow, 6*(3), 214–228.

Wang, Y., Li, M., Chen, J., Lei, J., Tao, Z., Xu, Q., & Liu, H. (2025). CFD-DEM study on effect of particle property on solid-liquid two-phase flow structure in a centrifugal pump under stall conditions. *Powder Technology, 458*, Article 121003.

Wang, K., Liu, H., Wang, L., Guo, P., Wang, Y., & Yang, J. (2024). Effect of particle size on vortex structure and erosion behavior of semi-open centrifugal pump. *Energy, 293*, Article 130576.

Wang, Z., & Qian, Z. (2017). Effects of concentration and size of silt particles on the performance of a double-suction centrifugal pump. *Energy, 123*, 36–46.

Wu, M., Zhang, J., Gui, N., Zou, Q., Yang, X., Tu, J., Jiang, S., & Liu, Z. (2024). Advances in the modeling of multiphase flows and their application in nuclear engineering—A review. *Experimental and Computational Multiphase Flow, 6*(4), 287–352.

Xiao, S., Wan, C., Zhu, H., Zhou, D., Hu, J., Bao, Y., Cao, K., & Zhao, K. (2025). Deep learning-based reconstruction of three-dimensional particle volume fraction fields in solid-liquid two-phase pipe flow from single cross-sectional data. *Powder Technology*, Article 121616.

Xie, H., Luo, X., Feng, J., Zhu, G., & Wang, L. (2024). Energy performance and flow characteristics of a pump-turbine under pump mode at different guide vane openings. *Journal of Energy Storage, 97*, Article 112743.

Yakovlev, A. Y., Sokolov, M. A., & Marinich, N. V. (2011). Numerical design and experimental verification of a rim-driven thruster. In *Proceedings of second international symposium on marine propulsors* (pp. 396–403).

Yan, X., Liang, X., Ouyang, W., Liu, Z., Liu, B., & Lan, J. (2017). A review of progress and applications of ship shaft-less rim-driven thrusters. *Ocean Engineering, 144*, 142–156.

Yasser, E., Zhou, L., & El-Emam, M. A. (2025a). CFD–DEM analysis of erosion in 90° elbow pipe induced by different particle shapes. *Powder Technology*, Article 121453.

Yasser, E., Zhou, L., & El-Emam, M. A. (2025b). Failure mechanism analysis of erosion in centrifugal pumps attributed to particle morphology: A coupled CFD–DEM–ANN approach. *Engineering Failure Analysis*, Article 109957.

Zhai, S., Jin, S., Chen, J., Liu, Z., & Song, X. (2022). CFD-based multi-objective optimization of the duct for a rim-driven thruster. *Ocean Engineering, 264*, Article 112467.

Zhang, Z., Liu, B., Ouyang, W., Zheng, R., & Vanierschot, M. (2025). Analysis of the energy loss mechanism of a rim-driven thruster under open water conditions. *Ocean Engineering, 319*, Article 120203.

Zhu, Z. (2014). Characteristic correlation between propellers cavitating wake and cavitation noise. *Applied Acoustics, 81*, 31–39.